

**Numerical Evaluation of Equivalence Ratio Measurement
Using OH* and CH* Chemiluminescence in Premixed and Non-Premixed
Methane-Air Flames**

C. S. Panoutsos, Y. Hardalupas*, A.M.K.P. Taylor

Department of Mechanical Engineering

Imperial College London

Exhibition Road, London SW7 2BX, United Kingdom

* Corresponding author:

Dr. Y. Hardalupas
Department of Mechanical Engineering
Imperial College London
Exhibition Road
London SW7 2BX
United Kingdom
Tel: +44 20 7594 7057
Fax: +44 20 7823 8845
E-mail: y.hardalupas@imperial.ac.uk

Abstract

This work presents results from detailed chemical kinetics calculations of electronically excited OH ($A^2\Sigma$, denoted as OH*) and CH ($A^2\Delta$, denoted as CH*) chemiluminescent species in laminar premixed and non-premixed counterflow methane-air flames, at atmospheric pressure. Eight different detailed chemistry mechanisms, with added elementary reactions that account for the formation and destruction of the chemiluminescent species OH* and CH*, are studied. The effects of flow strain rate and equivalence ratio on the chemiluminescent intensities of OH*, CH* and their ratio are studied and the results are compared to chemiluminescent intensity ratio measurements from premixed laminar counterflow natural gas-air flames. This is done in order to numerically evaluate the measurement of equivalence ratio using OH* and CH* chemiluminescence, an experimental practice that is used in the literature. The calculations reproduced the experimental observation that there is no effect of strain rate on the chemiluminescent intensity ratio of OH* to CH*, and that the ratio is a monotonic function of equivalence ratio. In contrast, the strain rate was found to have an effect on both the OH* and CH* intensities, in agreement with experiment. The calculated OH*/CH* values showed that only five out of the eight mechanisms studied were within the same order of magnitude with the experimental data. A new mechanism, proposed in this work, gave results that agreed with experiment within 30%. It was found that the location of maximum emitted intensity from the excited species OH* and CH* was displaced by less than 65 and 115 μm , respectively, away from the maximum of the heat release rate, in agreement with experiments, which is small relative to the spatial resolution of experimental methods applied to combustion applications, and, therefore, it is expected that intensity from the OH* and CH* excited radicals can be used to identify the location of the reaction zone. Calculations of the OH*/CH* intensity ratio for strained non-premixed counterflow methane-

air flames showed that the intensity ratio takes different values from those for premixed flames, and therefore has the potential to be used as a criterion to distinguish between premixed and non-premixed reaction in turbulent flames.

Keywords

OH* and CH* Chemiluminescence, Equivalence Ratio Measurement, Strain Rate, Premixed, Non-Premixed, Counterflow, Heat Release Rate, methane oxidation scheme, excited species sub-mechanism.

Introduction

Chemiluminescence from primarily premixed flames is widely used in a variety of combustion applications due to its natural occurrence in the flame - there is no need for external illumination - and of its easy exploitation in the harsh environments encountered, since it is an optical and therefore non-intrusive diagnostic [1]. It has been used for identification of the reaction zone [2], to compute Rayleigh index maps [3], as a marker of heat release rate [4-6], and to measure flame equivalence ratios [7-12]. By use of a Cassegrain optics-based *Chemiluminescence Sensor* (CS), similar to that used by Akamatsu *et al.* [13] & Kojima *et al.* [2], Hardalupas and Orain [7] demonstrated in their chemiluminescence study that the intensity ratio of the two excited radicals OH* and CH* is independent of strain rate in premixed counterflow flames at atmospheric pressure, in contrast to that of OH* and C₂*, which is a function of strain rate.

Despite the broad use of chemiluminescence as combustion diagnostic, there has been limited research effort involving modelling of its formation and destruction. Dandy and

Vosen [14] were the first to model the formation of OH* chemiluminescence. Their results showed good agreement with their experiment for lean premixed methane-air flames, however they did not consider CH* chemiluminescence. Walsh *et al.* [15] proposed a mechanism that also considered both CH* chemiluminescence and their calculations showed moderate agreement between measured and computed OH* mole fraction for a lifted laminar axisymmetric non-premixed flame. However, Walsh *et al.* [15] misused the rate constant measured by Berman *et al.* [16] by misallocating the entire product branch of the reaction of CH with molecular oxygen to OH*. Luque *et al.* [17] drastically improved the performance of the excited species mechanism proposed by Walsh *et al.* [15] by changing the OH* formation rate constant measured by Berman *et al.* [17] with the one measured by Porter *et al.* [18]. Docquier *et al.* [19] in their study of OH*, CH* and C₂*chemiluminescence a steady, one-dimensional flame under lean conditions and elevated pressure up to 10 bar at, used two kinetic schemes representing C₁ and C₂ hydrocarbons, coupled with the OH* and CH* chemiluminescence sub-model of Walsh *et al.* [15]. Measured and calculated OH* and CH* chemiluminescence profiles were in good agreement, for the range of examined pressures. Some discrepancies were observed at higher equivalence ratio values, but this – according to the authors – was due to the inability of the kinetics to predict the rich-flame behaviour. Higgins *et al.* [20, 21] studied the OH* and CH* chemiluminescence experimentally in fuel-lean, high-pressure (up to 25 bar), premixed, laminar methane-air flames and modelled OH* chemiluminescence [20] using a mechanism which comprised the OH* chemiluminescence sub-mechanism of Dandy and Vosen [14] and the methane-oxidation sub-mechanism from GRI-Mech 2.11 [22], excluding however all nitrogen chemistry. Their numerical results showed poor agreement with experiment, but they managed to predict the general trends of OH* chemiluminescence as a function of pressure. Smith *et al.* [23] in their study of a flat premixed sub-atmospheric methane-air flame proposed an excited-species mechanism that

accounted for the formation of OH* and CH*. Though they calibrated their mechanism by using broad-band detection for CH* (380-450 nm) in their experiments, the authors claimed that an overestimation of no more than 20% was expected. Kojima *et al.* [24] studied OH*, CH* and C₂* chemiluminescence both experimentally and numerically using a mechanism comprised GRI-Mech 3.0 [25] and the OH* and CH* excited species mechanism of Walsh *et al.* [13]. Their results showed reasonable agreement in terms of shape, peak location, emission zone thickness and peak intensity variation of the chemiluminescent profiles of a two-dimensional laminar premixed flame for lean and stoichiometric conditions. They also presented results on the stoichiometry dependence of the OH*/CH* intensity ratio, but they did not study the effect of the strain rate.

As can be seen in the literature review on OH* and CH* chemiluminescence modelling presented above, there is a lack of modelling results concerning the effect of equivalence ratio coupled with the effect of strain rate on OH* and CH* chemiluminescence. This effect of strain rate is important for attempts to monitor the local equivalence ratio of flames in combustion applications by measuring the chemiluminescent emission from these two flame radicals, as it has been shown by Hardalupas and Orain [7]. Indeed, the chemiluminescence modelling efforts in the literature have been performed using steady, freely propagating flames for which the effect of strain rate cannot be quantified.

The purpose of this paper is to numerically evaluate the equivalence ratio measurement using OH* and CH* chemiluminescence in premixed and non-premixed methane-air flames. The performance of different detailed-chemistry methane mechanisms that account for the formation and destruction of the chemiluminescent species OH* and CH*, and the effect of equivalence ratio and strain rate on the chemiluminescent intensity emitted from the excited species OH* and CH*, and their ratio, in premixed laminar methane-air flames at atmospheric pressure, will be studied. In order to study the effect of strain rate,

we consider a counterflow flame geometry. The computational results are compared with measured absolute OH*/CH* intensity ratio data [26] and the validity of using the chemiluminescent intensity of OH* and CH* as heat release rate markers will be assessed. The chemistry model reported by this study can be used to study the effect of high pressure, preheating and different fuels encountered in a real combustion application, on the OH*/CH* ratio used to measure equivalence ratio.

Geometry and Excited Species Mechanisms

In order to study the effect of strain rate along with that of equivalence ratio, ϕ , we simulated the counterflow laminar flame geometry using the one-dimensional flame code OPPDIF [27] of Chemkin [28] to solve for velocity, temperature and species concentrations along the centerline of premixed and non-premixed counterflow methane-air flames [29]. The *strain rate*, a , in the counterflow geometry is defined as $a = 2V_o / H$, where V_o is the bulk velocity of the fuel-air mixture at the exit of the nozzles. The same geometry was used during our experiments [26], so results from our simulations will be comparable to experimental ones. A schematic of the premixed counterflow geometry showing the two counterflow premixed methane-air flames is presented in Fig. 1. OPPDIF can compute the premixed flames between two opposing nozzles. A similarity transformation reduces the flow field to a one-dimensional problem. For the radially axisymmetric case, the similarity solution assumes that the radial component of velocity changes linearly with radius and that the dependent variables become functions of the axial direction only. Details of the OPPDIF similarity solution for counterflow premixed methane-air flames are provided by Kee *et al.* [30].

In order to model chemiluminescence, reactions that describe the formation and destruction of the excited species OH* and CH* were added to detailed methane oxidation

schemes. The destruction of the excited species occurred either by spontaneous emission – *chemiluminescence* – or by collisional relaxation from the excited to the ground state – *quenching*. The currently accepted production path of OH*, given in reaction R1, was proposed by Gaydon [31] and was later supported by the experimental work of Krishnamachari and Broida [32] on acetylene/atomic oxygen flames. The results of the experiments of Krishnamachari and Broida [32] on acetylene were supported by those of Bowman and Seery [33], who performed shock tube experiments to study chemiluminescence in CH₄/O₂ mixtures. The rate constant for that reaction was derived by Porter *et al.* [18] by correlating measured CH, O₂ and OH* profiles through the flame. Walsh *et al.* [15] reported a rate constant for the OH* formation that was two orders of magnitude greater than the one derived by Porter *et al.* [18], although Grebe and Homann [34], in the same year, reported a rate constant approximately equal to the one derived by Porter *et al.* [18] in their work at a flow reactor. Smith *et al.* [23] proposed a rate constant for OH* formation three times greater than that of Porter *et al.* [18] by measuring absolute excited concentrations of OH* at a flat premixed low-pressure methane-air flame. Haber and Vandsburger [35] have proposed the reaction of HCO with O as a formation path for OH* chemiluminescence. This formation path has been rejected in the literature because of the lack of energy release to produce the excited OH* radical and also because that path shows very little variation with stoichiometry, in contrast to the observations of Smith *et al.* [23]. Carl *et al.* [36] presented the first evidence that the emission intensity of OH* chemiluminescence is indeed directly proportional to the local concentration of CH and O₂ and measured a reaction rate coefficient for OH* formation having a value nearly the same as the one determined by Porter *et al.* [18], at a temperature range of 300-550K.



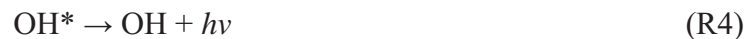
Smith *et al.* [37] determined the rate constants for two additional formation paths of OH* based on experiments at low pressure H₂-air and CH₄-N₂O flames:



to be equal to $k_2 = 5.45 (\pm 2.3) \times 10^{12}$ and $k_3 = 1.45 (\pm 0.6) \times 10^{15} \text{ cm}^6/(\text{mol}^2\text{s})$. These reactions are important mainly H₂-air flames.

Most recently Hall and Petersen [38] reported on new experimental data for the rate constants of reaction R1 and of the additional formation paths proposed for OH*, R2 and R3. The measured rate constant for OH* formation, reported by Hall and Petersen [38], through reaction R1 was $k_1 = 3.24 \times 10^{14} T^{-0.4} \exp(-4150/RT) \text{ cm}^6/(\text{mol}^2\text{s})$ which is one order of magnitude greater than the value reported in their earlier work [39] and more than three orders of magnitude greater than that of Porter *et al.* [18]. The reported rate constant for reaction R2 was $k_2 = 3.1 \times 10^{14} \exp(-10000/RT) \text{ cm}^6/(\text{mol}^2\text{s})$ and they recommended the use of the two step formation mechanism that does not include R3. Their shock-tube experiments were performed in mixtures of H₂/O₂/Ar, CH₄/O₂/Ar, and CH₄/H₂/O₂/Ar with high levels of argon dilution at high temperatures ($1200 < T < 2200\text{K}$) and at atmospheric pressure.

The heat of formation of OH* has been reported to be 93 kcal/mol above of that of the ground-state OH [15]. Spontaneous chemiluminescent emission (R4) and collisional quenching data for OH* (see Tables 1-6) have been reported by Tamura *et al.* [40].



Research by Glass *et al.* [41] first introduced the reaction of *ethynyl radical*, C₂H, with atomic oxygen as a source for CH* (R6). Experiments and modeling performed by Joklik *et al.* [42] then showed that, although the reaction of C₂H with molecular oxygen (R5) may contribute to CH* formation, the dominant source of CH* appears to be the reaction of C₂H with atomic oxygen. Devriendt *et al.* [43] were the first to present unambiguous evidence that a major, if not the dominant, source of CH* is the reaction of the ethynyl radical with atomic oxygen (R6). Devriendt *et al.* [44] confirmed the results found by Joklik *et al.* [42] and measured the rate constants as $k_5 = 3.6 \times 10^{-14} \text{ cm}^3 \text{ mol}^{-1} \text{ s}^{-1}$ and $k_6 = 1.8 \times 10^{-11} \text{ cm}^3 \text{ mol}^{-1} \text{ s}^{-1}$, with an estimated uncertainty of around 40%. Smith *et al.* [37], after performing experiments at low pressure H₂-air and CH₄/N₂O flames, measured the rate constants for the two formation paths of CH*, reactions R5 and R6, to be equal to $k_5 = 3.20(\pm 1.0) \times 10^{11} \exp(-805/T)$ and $k_6 = 2.50(\pm 0.8) \times 10^{12} \text{ cm}^3 / (\text{mol s})$, the latter one being 40% of their previous reported value [23]. Recently, Elsamra *et al.* [45] studied the temperature dependence of the rate constant of reaction R5 over the temperature range 316 – 837 K, using pulsed laser photolysis techniques. They reported that the rate constant has a positive temperature dependence given by $k(T) = AT^{4.4} \exp(1150 \pm 150/T)$, where $A = 1 \times 10^{-27} \text{ cm}^3 \text{ s}^{-1}$. They concluded that reaction R5 contributes significantly to CH* chemiluminescence in hot flames and especially under fuel-lean conditions where it probably dominates reaction R6.

Spontaneous chemiluminescent emission (R7) and collisional quenching data (Tables 1-6) for CH* have been reported by Tamura *et al.* [40]. The heat of formation of CH* has been reported to be 66.3 kcal/mol above that of ground-state CH [15], based on the energy of the spontaneously emitted photon.



The mechanisms studied in this paper contain a detailed chemistry methane oxidation mechanism and an additional sub-mechanism that accounts for the formation and destruction of the chemiluminescent species OH* and CH*. Seven different mechanisms were studied:

1. The first one included the excited species sub-mechanism proposed by Walsh *et al.* [15], coupled with the detailed chemistry mechanism of methane oxidation GRI-Mech 2.11 (*Mechanism 1*).
2. The second consisted of the Smith *et al.* [23] and Luque *et al.* [45] starting excited species sub-mechanism coupled with GRI-Mech 3.0 (*Mechanism 2*).
3. The third consisted of the Smith *et al.* [23] and Luque *et al.* [46] proposed optimized excited species sub-mechanism coupled with GRI-Mech 3.0 (*Mechanism 3*).
4. The fourth one was the combination of the excited species sub-mechanism proposed by Luque *et al.* [17] with GRI-Mech 3.0 and not with GRI-Mech 2.11 as it was proposed in [16] (*Mechanism 4*).
5. The fifth mechanism included the methane oxidation scheme of Lindstedt *et al.* [47-49], coupled with the excited species sub-mechanism proposed by Luque *et al.* [17] (*Mechanism 5*).
6. The sixth mechanism consisted of GRI-Mech 3.0 and the excited species sub-mechanism of Table 5, where the new rate constants for CH* formation of Elsamra *et al.* [45] were used (*Mechanism 6*).
7. The seventh mechanism was the same as the sixth, except that the rate constant for OH* formation of Carl *et al.* [36] was used (Table 6) (*Mechanism 7*).

All the excited species sub-mechanisms of the mechanisms 1-7 studied in this paper are listed in Tables 1-6. Details of the methane oxidation scheme and the excited-species sub-mechanism used for each of the different mechanisms studied in this work can be seen in Table 7.

Following the work of Dandy and Vosen [14], we included in the studied chemiluminescence mechanisms 4, 6 and 7, the additional elementary reactions where OH^* and CH^* react and form products just as ground-state OH and CH do. As expected, no measurable difference in the results obtained with or without the addition of these elementary reactions was found, due to the low concentrations of the excited species; these results are not reported here. The assumption that the products of reactions of the excited species will be the same as those of the ground-state counterparts, does not affect the conclusions of this work because the concentrations of the excited species and their products are so low that they have little impact on the overall flame chemistry.

The thermochemical and transport coefficients data used for mechanisms 1 and 4-7 were the ones provided with GRI-Mech 3.0, with the addition of the respective thermochemical data for the excited species OH^* and CH^* , which were calculated with Chemkin [28], using data for the heat of formations of OH^* and CH^* taken from Walsh *et al.* [15]. The thermochemical data for mechanisms 2 and 3 were provided by G. P. Smith [50]. The thermodynamic and transport data for mechanism 5 were obtained from ref. [51]. The transport coefficients for the excited species were the same as those of the ground state species.

Selection of Operating Conditions

The geometry used for the calculation of the laminar premixed and non-premixed counterflow flames using OPPDIF is shown in Fig. 1. The nozzle separation distance, H , was always equal to 2.5 cm, the same as set during our experiments where the *Chemiluminescence Sensor* was used to measure OH^* and CH^* chemiluminescent intensity emitted from the premixed methane-air counterflow flames [7,26]. Numerical results were obtained for an equivalence ratio range from $\phi = 0.6$ to $\phi = 1.3$, as in the experiment, and a strain rate range from $80 - 400 \text{ s}^{-1}$, corresponding to air-fuel mixture area-averaged (bulk) velocities at the nozzles $V_o = 1-5 \text{ ms}^{-1}$. The range of the bulk velocity of air-fuel mixture during our experiments was $V_o = 1.5 - 4 \text{ ms}^{-1}$. The experimental uncertainty for the measurements presented in this work was less than $\pm 5\%$. Whenever natural gas was used as the fuel instead of pure methane, its composition was: 93.5% CH_4 , 3.5% C_2H_6 , 0.7% C_3H_8 , 0.22% C_4H_{10} , 0.065% C_{5+} , 1.5% N_2 & 0.5% CO_2 . More details concerning the experiment can be found in [7,26].

The conditions for the calculations were as follows: the pressure was always equal to 1 atm and the temperature of the fuel-air mixture was set to $T = 300\text{K}$, except for $\phi = 0.60$ & 1.30 and strain rate values of $a = 240-400 \text{ s}^{-1}$, for which extinction occurred requiring the temperature to be increased to $T = 400 \text{ K}$ to obtain a solution. The standard transport model of Chemkin has been used in the calculations and details can be found in [27,30]. Mixture-averaged coefficients were used in order to compute transport coefficients.

The absolute convergence criteria for the Newton iteration and time stepping, used for the OPPDIF calculations, were 1×10^{-13} and 1×10^{-6} respectively. A coarse mesh of 50 evenly spaced points was used for the initial grid, and then more points were automatically added by OPPDIF into the regions of large gradient or curvature in the solution. The final mesh had

more than 300 points for each solution. We minimized the computational time by using an initial converged solution as an initial guess for a calculation with slightly different conditions (ϕ or strain rate).

Description of the Optical Detection System

The chemiluminescence detection system comprised a focused Cassegrain-based optical sensor based on mirrors, thus reflective elements, avoiding chromatic aberrations for different wavelengths. The sensor used in the context of this work had a 300 mm working distance with diameters of primary and secondary mirrors of 150 and 50 mm, respectively. This ensured a probe volume with nominal diameter of 200 μm and length of 1.6 mm. The spatial resolution of the Chemiluminescence Sensor (CS) was found to be of the order of its probe volume (200 μm x 1.6 mm) and has been thoroughly evaluated at laminar Bunsen and turbulent swirl-stabilised flames, using OH PLIF and Reaction Rate Imaging [26].

The collected light from the CS is focused onto a pinhole placed in front of an optical fiber (with core diameter 200 μm and Numerical Aperture of 0.2), which is connected to a purpose-built Spectroscopic Unit. The light is split up into two spectral fractions using two dichroic mirrors (Optical Coatings Japan) with efficiencies greater than 95%. Each part is directed onto appropriate interference filters (Optical Coatings Japan) specific to the radical considered, at 308.5 nm for the OH* and 430.5 nm for the CH*, with corresponding efficiencies of 22.0% and 45.3% and with bandwidths of 18.0 nm and 1.9 nm, respectively. The collected light intensities are transformed into electrical signals using two photomultipliers (PMTs) (Hamamatsu R269), one for each radical considered, always supplied with the same level of voltage (gain). The temporal signals of OH* and CH* are then filtered, using passive low-pass filters (TTE) with 8 kHz cut-off frequency, and digitised

using a 12-bit (PCI-MIO-16E-1, National Instruments) high-sampling rate A/D card. The sampling frequency f_s was always equal to 50 kHz for the laminar flames studied in this work. Care was taken to operate the PMTs at a range of supply voltage optimised to maintain linearity of output voltage with respect to input signal; all experiments were performed at selected conditions to produce peak voltages within the range of PMT linearity.

The experimental data presented in the past by Hardalupas and Orain [7] represented measurements of relative intensity of OH^*/CH^* and not absolute values of the chemiluminescent intensity ratio. In order to compare our experimental findings with results from modelling our detection system used to measure OH^* and CH^* chemiluminescence had to be calibrated to account for the differences in the optical system's responsivity at different spectral bands, as suggested by Nori and Seitzman [52]. This calibration was performed using a Xe calibration lamp. The calibration lamp emits light with a known spectral response. By measuring with our optical system the intensity ratio at the two specific bands, related to OH^* and CH^* , emitted from the calibration lamp and comparing this with the calibration data, we can calculate an absolute scale factor needed to correct for the optical system's responsivity at the OH^* and CH^* spectral bands. More details concerning the calibration of the optical sensor can be found in the Appendix.

Results and Discussion

The experimental results presented in this work are ratios of chemiluminescent intensity for the excited-state species OH^* and CH^* , integrated across the probe volume of our optical sensor and not absolute molar concentrations of the excited species. The geometry of the flame at the counterflow burner resembles a disk (Fig.1); therefore the probe volume of the sensor was focused vertically at the centerline of the burner inside the reaction zone of the

flame (location of maximum collected chemiluminescence signal). The collected signal contained the region of the flame located inside the probe volume of the sensor [26]. The ratio of the maximum chemiluminescence intensities measured at the reaction zone of the counterflow flame is compared to the ratio of the maximum calculated photon emission rates for OH* and CH* (Reactions R4 and R7) and not to the molar concentrations derived from our calculations.

The calculated intensity distributions for OH* and CH* radicals were not integrated over the size of the probe volume of the Cassegrain optics. This approach does not influence the results for two reasons: (a) the shape of the two intensity distributions is the same; (b) the width of both intensity distributions is narrower than the size of the probe volume. As a consequence, integration over both intensity distributions will not change the value of the calculated intensity ratio OH*/CH*, which was calculated from the two maxima.

Premixed Methane-Air Flames

In order to explore the effect of the presence of the additional reactions that describe the formation and destruction of the chemiluminescent species OH* and CH* on the gross characteristics of the solutions obtained here and to ensure that the numerical solutions presented are consistent with published experimental data, the laminar flame speeds, temperature and species concentrations were calculated for the unmodified GRI-Mech 3.0 and compared with the results obtained using mechanism 4. Mechanism 4 was selected because, first, its excited species sub-mechanism has been thoroughly tested [16], and second, its methane oxidation scheme (GRI-Mech 3.0) was converging faster to a solution. It is expected, however, that any other mechanism would have given the same qualitative results with mechanism 4.

The laminar flame speeds were calculated for a range of ϕ values from 0.6 to 1.4, as displayed in Fig. 2, using PREMIX of Chemkin [28] and were compared to the experimental results of Egolfopoulos *et al.* [53]. On the same graph, the laminar flame speeds calculated by the unmodified GRI-Mech 3.0 mechanism are plotted in order to study the effect of the added reactions to the mechanism. As expected, the results from the calculations for the two mechanisms coincide, since the concentrations of the chemiluminescent species are so small that do not affect the overall methane combustion chemistry. In terms of the comparison with the experimental results, it can be seen that the numerical results from GRI-Mech 3.0 and the proposed excited species mechanism agree very well with the experimental results of Egolfopoulos *et al.* [53] for $\phi \leq 1.0$. For $\phi > 1.0$ the results from the calculation display a small underestimation of the flame speed.

Temperature, heat release rate and species concentrations computed with OPPDIF using mechanism 4 are compared with results from the unmodified GRI-Mech 3.0 in Fig. 3a&b, for a $\phi = 0.70$ and a $a = 80 \text{ s}^{-1}$ counterflow premixed methane-air flame. It can be seen that the addition of excited species elementary reactions did not affect the flame structure in terms of heat release rate, temperature distribution and major mole fractions. Furthermore, the precursors of OH* and CH*, CH and C₂H respectively, are not significantly affected by the added reactions, since the maximum mole fraction of the excited species are 1.604×10^{-11} and 1.378×10^{-12} , for OH* and CH* respectively.

Axial centreline major and chemiluminescent species mole fraction profiles are depicted in Fig. 4 for $\phi = 0.70$ and a $a = 320 \text{ s}^{-1}$, to show the general structure of the laminar premixed counterflow flames. The results have been obtained using mechanism 4. The location of the “*twin flames*” can be clearly identified by the peaks in the profiles of CH, OH* and CH*. The ground-state OH profile is wider, since ground-state OH is not short-lived and can be found in the post-flame gases as well [54].

To investigate whether the excited species OH* and CH* can be used as heat release rate markers, we plotted the calculated (using mechanism 4) mole fraction profiles of OH* and CH*, along with the profiles of the *formyl radical*, HCO, *formaldehyde*, CH₂O, *hydroxyl*, OH and their product, [OH] x [CH₂O] and of the *heat release rate*, Q , for the flame shown on the lower side of Fig. 4. The formyl radical was chosen because it has been suggested in the literature that it can be used to mark very well the heat release rate [4,5,55]. Unfortunately, single-shot LIF measurements of HCO distributions in turbulent flows seem not to be feasible [55,56] and Paul *et al.* [55] have shown that the product of OH and CH₂O concentrations is directly proportional to the reaction rate of CH₂O + OH → H₂O + HCO and, therefore, yields an estimate for the production rate of HCO. The calculated peak-to-peak distances between the species mole fraction profiles and the heat release rate, for $\phi = 0.70$ and $a = 320 \text{ s}^{-1}$, are approximately 10 μm for HCO, 16 μm for the product of OH and CH₂O, 30 μm for OH* and 70 μm for CH*, Fig. 5. These peak-to-peak distances were calculated for all the conditions studied in terms of equivalence ratio and strain rate, and the results using mechanism 4 can be seen in Fig. 6a [57]. The peak-to-peak distances were below 20 μm for HCO, below 35 μm for the product of OH and CH₂O, between 20-65 μm for OH* and between 55-115 μm for the CH* excited radical, shown in the histograms of Fig. 6b. The observation concerning the formyl radical agrees well with the results of Najm *et al.* [4,5]. These results show that the chemiluminescent species OH* and CH* can be used as heat release rate markers, especially OH*, since the distance between the peak observed in the heat release rate profile and their maximum intensity is smaller than the spatial resolution of most optical devices used to measure chemiluminescence in flames, including the Chemiluminescence Sensor used during our experiments. OH* chemiluminescence, in particular, exhibits the same performance as a heat release rate marker as the product of OH and CH₂O, since the difference between their peak concentrations is less than 15 μm . These numerical results agree well with results from

experiments performed at laminar hydrocarbon-fuelled Bunsen flames [57], where OH* and CH* chemiluminescent intensity peaks found to coincide with the heat release rate peaks measured with simultaneous OH and CH₂O PLIF. The calculated peak-to-peak distances between the species mole fraction profiles and the heat release rate, were independent of the strain rate, as can be seen in Fig. 7a. The equivalence ratio had a small effect only for rich stoichiometries $\phi = 1.20$ and 1.30 , mainly for CH* and less on OH*, Fig. 7b. The better correlation of OH* with the heat release rate has also been reported by Najm *et al.* [4].

The sequence of the location of peak intensities for the OH* and CH* excited radicals, is OH* followed by CH*, as one scans the flame from the reactants (lower part of Fig. 5) to the products (upper part of Fig. 5). This result agrees well with the experimental and computational results of Kojima *et al.* [2,24,58], who reported the same sequence of chemiluminescent species profiles, and measured in a laminar methane-air flame a distance between OH* and CH* peak intensities of $50 \mu\text{m}$, which is in good agreement with the distance of $40 \mu\text{m}$ calculated using mechanism 4.

Fig. 8a presents the calculated maximum values of heat release rate and OH* chemiluminescent intensity as a function of equivalence ratio, with strain rate as parameter, for mechanism 4. We clarify that the chemiluminescent intensity of OH* and CH* is found by first calculating the *Rate Of Production* (ROP) of reactions R4 & R7 and then normalising it by its maximum calculated value. This calculated quantity represents the experimentally measured chemiluminescent intensity. The relative loss rate is assumed to be negligible. In Fig. 8a, the lines represent the maximum calculated chemiluminescent intensity and the symbols the maximum heat release rate. The OH* chemiluminescent intensity increases monotonically with ϕ for all values of a, for $0.6 \leq \phi < 1.1$, and decreases monotonically with increasing ϕ thereafter. These results agree qualitatively with our experimental results [26], Fig. 8b, and also with the results from calculations and experiments of Dandy and Vosen [14],

although they did not study the effect of the strain rate. According to the results of the calculations in the present study, the strain rate does not seem to have an effect either on the heat release rate or the chemiluminescent intensity, for the lean range of ϕ , $0.6 \leq \phi < 0.9$, but there is an effect of strain rate on both calculated quantities on the rich side of ϕ , $\phi > 0.9$. In contrast, the results of experiments, Fig. 8b, show that there is an effect of the strain rate for all the range of ϕ studied. The location of the measured maximum OH* intensity was at $\phi = 1.0$ and the calculated one was for $\phi = 1.1$, coinciding with the maximum laminar flame speed (Fig. 2). The maximum calculated OH* intensity correlates well with the maximum heat release rate, for all values of strain rate, so this fact supports the argument that OH* chemiluminescence can be used as heat release rate marker.

Maximum values of calculated heat release rate and normalised CH* intensity are plotted as a function of equivalence ratio, with strain rate as a parameter, in Fig. 9a, for mechanism 4. The trends observed for the CH* intensity are the same as for OH*, although CH* intensity does not follow so well the trend of heat release rate for $0.6 \leq \phi < 0.9$. The calculated maximum values of CH* chemiluminescence as a function of ϕ , with the strain rate as a parameter, have the same trend with equivalence ratio with our experimental data, shown in Fig. 9b. As was observed for OH*, the maximum measured CH* intensity was for $\phi = 1.0$ and the calculated one was for $\phi = 1.1$. CH* chemiluminescent intensity correlates well with the calculated maximum values of heat release rate, so CH* can be used as heat release rate marker, although OH* intensity should be preferred in lean premixed flames.

The reason for the calculation of the ratio of OH*/CH* chemiluminescent intensity is that this ratio has been used experimentally to measure equivalence ratio in premixed natural gas-air flames, as it has been shown by Hardalupas and Orain [7]. The results of the calibration experiments for premixed natural gas-fuelled flames, at atmospheric pressure, performed at the counterflow burner are shown in Fig. 10. The depicted values are the

absolute measured OH*/CH* intensity ratios as a function of equivalence ratio, having the strain rate as a parameter. These results show that the OH*/CH* intensity ratio has a monotonic dependence on equivalence ratio and there is no effect of strain rate. The same qualitative results have been obtained when pure methane was used as the fuel, although the OH*/CH* ratio was approximately 20% higher for lean fuel and air mixtures and less than 10% higher for stoichiometric and rich mixtures [26].

The computed OH*/CH* chemiluminescent intensity ratio is equal to the ratio of the maximum values of the ROP of the reactions R4 and R7, encountered at the reaction zone. The results of the calculations are plotted in Fig. 11a-g for the seven mechanisms studied, respectively, where the OH*/CH* chemiluminescent intensity ratio is plotted as a function of equivalence ratio, with the strain rate as a parameter. Both the experimental results (Fig. 10) and those from the calculations for the seven mechanisms studied so far (Fig. 11), show that the OH*/CH* ratio monotonically decreases as the equivalence ratio increases, with no dependence on the strain rate. There is, therefore, good agreement between calculations and experiment, in terms of the trend of the OH*/CH* ratio as a function of equivalence ratio, for all the mechanisms studied in this work.

However, quantitatively, there is a disagreement between the calculated and measured absolute values of the OH*/CH* intensity ratio, as can be seen in the magnitude of the gradient of the curves. This discrepancy is observed for all mechanisms studied and only for mechanisms 4 -7 the calculated and measured values of the OH*/CH* ratio are of the same order of magnitude. In terms of mechanism 1, the calculated results are three orders of magnitude greater than experiment and this is mainly due to the different rate constant used for the OH* formation (the rate constant used by Walsh *et al.* [15] in mechanism 1 is 541 times greater than the one used by Porter *et al.* [18] in mechanism 4), since as seen in Tables 1 & 4 the rest of the excited species sub-mechanisms are the same. The fact that the excited

species sub-mechanisms of Tables 1 & 4 are coupled with GRI-Mech 2.11 & 3.0, respectively, do not affect the results significantly.

The starting excited species sub-mechanism reported by Smith *et al.* [23] coupled with GRI-Mech 3.0, mechanism 2, is the only one that shows a linear relationship between the calculated OH*/CH* intensity ratio and stoichiometry, in contrast to all the other mechanisms studied in this work and the results of experiment that show an exponential decay of OH*/CH* with increasing stoichiometry values (Fig. 11b). Mechanism 2 is the only mechanism for which the calculated OH*/CH* ratio is less than unity due to the additional CH* formation paths (reactions 8 & 10, Table 2) coupled with the additional C and C₂ chemistry (reactions 1-6, Table 2 & 3). When these additional CH* formation paths are removed and the OH* rate constant is tripled, as suggested by Smith *et al.* [23] in their optimised mechanism (mechanism 3 in this work), the calculated OH*/CH* ratio is overestimated by more than 10 times from our experimental data (Fig. 11c). However, it should be noted that Smith *et al.* have published new rate constants for CH* formation, that include CH* formation through reaction R5, in their recent work [37]. The performance of these rate constants has not been tested in the context of this work.

The results from calculations with mechanisms 4 and 5 are shown in Figs. 11d&e. The two mechanisms have the same excited species sub-mechanism (Table 4), and the reason for using them is to test the performance of two different detailed methane oxidation schemes: GRI-Mech 3.0 [25] and Lindstedt *et al.* [47-49]. The results obtained with mechanism 5 showed the best quantitative agreement compared to the experimental ones, and the results obtained with mechanism 4 agreed reasonably well with the experimental data. A solution could not be converged using mechanism 5 for $\phi = 0.60$ and 1.20 and strain rate greater than 160 s⁻¹ and also when ϕ was equal to 1.30. The same phenomena were observed experimentally for methane-fuelled flames due to extinction occurring for lean mixtures and

flashback occurring when $\phi = 1.20$ & 1.30 [26]. The higher values of OH^*/CH^* calculated with GRI-Mech 3.0 (Fig. 11d) compared to the values obtained using the Lindstedt *et al.* mechanism (Fig. 11e), should be attributed to the overestimation of the precursor of OH^* , the *methylidyne* radical, CH, as has been reported by Gibaud *et al.* [65].

Mechanism 6 comprises GRI-Mech 3.0 and the excited species sub-mechanism suggested by Luque *et al.* [17], but, instead of the rate constants for CH^* formation of Devriendt *et al.* [44], the recently published rate constants of Elsamra *et al.* [45] are used (Table 5). The use of these new rate constants resulted in the increase of CH^* and decrease of the OH^*/CH^* intensity ratio by approximately 15% in comparison with mechanism 4 (Figs. 11d&f). The OH^*/CH^* intensity ratio calculated using mechanism 6, is overpredicted by approximately 2.5 times relative to the experimental measurements.

Substituting the OH^* formation rate constant of Porter *et al.* [18] with the one recently measured by Carl *et al.* [36] (Table 6), results in a further decrease of the calculated OH^*/CH^* intensity ratio, since OH^* chemiluminescence is reduced by approximately 30%. The results of mechanism 7, seen in Fig. 11g, agreed with the results of mechanism 5, although the OH^*/CH^* intensity ratio values calculated with the latter had a steeper gradient and are quantitatively closer to the experimental ones (approximately two times higher). In contrast, if the rate constant for OH^* formation (R1) recently proposed by Hull and Petersen [38] is used, results will be higher by at least two orders of magnitude in comparison with the results from mechanisms 4 - 7 and our experimental data [26] due to the overestimation of the OH^* chemiluminescence.

A small effect of strain rate is observed on the lean limit of equivalence ratio in the results obtained using mechanisms 4, 6 and 7. As can be seen in Figs. 11d,f&g, there is a spread of the calculated OH^*/CH^* intensity ratio values for $\phi = 0.60$ and 0.70 . This phenomenon is in agreement with the experimental results for natural gas fuelled premixed

counterflow flames shown in Fig. 10. The results obtained using mechanism 5 (Fig. 11e) do not show this spread of the OH*/CH values for lean values of ϕ , in agreement with the experiment, therefore it can be concluded that this phenomenon is due to the choice of the GRI-Mech 3.0 mechanism for modelling the methane chemistry.

By coupling the Lindstedt *et al.* [47-49] methane oxidation scheme with the excited species sub-mechanism of mechanism 7 (Table 6), we were able to obtain an improved quantitative agreement between the calculated OH*/CH* intensity ratio values and available experimental data. The results obtained with this mechanism (mechanism 8) are shown in Fig. 12 and are compared with experimental results from methane-air flames obtained for only one value of strain rate ($a = 240 \text{ s}^{-1}$) [26]. The results obtained with mechanism 8 showed the best qualitative and quantitative agreement between calculations and experiment for all the mechanisms studied in this work. The observed gradient of the calculated OH*/CH* values agreed well with the corresponding gradient of the experimental results for $\phi = 0.8 - 1.2$, although the experimental data were shifted at slightly higher values (Fig. 12). For $\phi = 0.7$ the results from calculations were approximately equal to the measured OH*/CH* values. However, the flame extinction observed experimentally for $\phi = 0.6$ was not reproduced in our simulation results. The spread of the calculated OH*/CH* values for lean values of ϕ observed at the results of mechanisms 4, 6 and 7, was not observed in the results of mechanism 8, as was the case for mechanism 5, further supporting the argument that this phenomenon was due to the use of GRI-Mech 3.0 mechanism for modelling the methane chemistry.

It is important to note, as indicated by one reviewer, that the comparison between the numerical results from the eight mechanisms studied in this work and the experimental results is very sensitive to the characteristics (i.e. centre wavelength, bandwidth, efficiency) of the interference filters used to measure OH* and CH* chemiluminescence. The choice of the

characteristics of these filters is critical to the measurement of the corresponding rate constants and the optimisation of the proposed mechanisms found in the literature, see for example the CH* rate constant measurement described by Smith *et al.* [23]. We selected filters with different bandwidths in the experiment to reflect the different bandwidth of the emitted light from OH* and CH* radicals and in this way maximize the collection of light emitted from each radical by minimizing the contribution from the background. However, care should be taken when comparing results obtained using different optical setups found in different experiments.

In addition, care should be taken when comparing the performance of different methane oxidation schemes due to the uncertainties of the studied mechanisms, particularly the large uncertainties associated with the chemiluminescence sub-mechanisms. One may not expect the main reason for the poor performance of some of the studied mechanism to be due to the choice of the methane oxidation scheme. This means that one cannot identify the best performer from several underlying methane oxidation mechanisms, based on a better fit to chemiluminescence data, since the likely reason for the disagreement probably is the excited-species mechanism.

Finally, it should be concluded that although the equivalence ratio and the strain rate have an isolated effect on both the calculated and the experimentally measured chemiluminescent intensity of OH* and CH*, as can be seen in Figs. 8 and 9, their ratio is not significantly affected by the strain rate, and has a monotonic dependence on ϕ , as observed in experiment (Fig. 10) and the results from calculations for all the mechanisms studied in this work (Fig. 11, 12). This shows that this ratio can be used to measure equivalence ratio in premixed natural gas and methane-air flames at atmospheric pressure, as was suggested in our previous work [7, 26, 59].

Non-Premixed Methane-Air Flames

The previous results have demonstrated that the intensity ratio OH^*/CH^* can be used to determine equivalence ratio in premixed flames. However, there are cases for which premixed and non-premixed flames may be present in a combustion application. Therefore, we would like to investigate the behavior of OH^*/CH^* in non-premixed flames in order to evaluate if this ratio can be used to distinguish between premixed and non-premixed flames. This evaluation cannot be performed experimentally because non-premixed flames produce soot, which emits strongly over a wide range of the flame's spectrum, including the CH^* band, and as a consequence the experimental quantification of the OH^* and CH^* intensities is difficult.

OH^* and CH^* chemiluminescence emitted by a non-premixed counterflow methane-air flame has been studied for different levels of strain rate. This was done in order to theoretically assess the effect of strain rate on the OH^*/CH^* chemiluminescent intensity ratio. Results of calculations for a non-premixed methane-air flame with strain rate $a = 40 - 280 \text{ s}^{-1}$, using excited species mechanism 4, are shown in Fig. 13. For strain rate values greater than 280 s^{-1} a solution could not be obtained for the non-premixed flame. Results show that, first, the calculated maximum values of OH^* chemiluminescence are much lower than the CH^* maxima and both are dependent on strain rate, and second, the calculated OH^*/CH^* intensity ratio is slightly affected by strain rate having a linear dependence. However, if the results for the non-premixed flame are plotted on the same graph with the corresponding results for the premixed flame (Fig. 14), we observe that the dependency on strain rate for the non-premixed flame is negligible.

In addition, we can observe in Fig. 14 that the calculated values of OH^*/CH^* for the premixed flame are approximately 5 - 50 times greater than the respective values for the non-premixed flame. This is due to OH^* chemiluminescence being much lower than CH^* for the

non-premixed flame. Therefore the OH*/CH* intensity ratio has the potential to be used as a criterion to decide if non-premixed or premixed combustion takes place inside a combustion application. This is very important because it indicates that the Chemiluminescence Sensor can be used to measure the equivalence ratio of the reacting mixture of partially-premixed flames, even when non-premixed reaction may also occur.

Furthermore, the calculated peak-to-peak distances between the maxima of the chemiluminescent species mole fraction profiles and the heat release rate, were calculated for the non-premixed flame with different values of strain rate ($a = 40 - 280 \text{ s}^{-1}$). The peak-to-peak distances were approximately between 0-22 μm for OH* and between 21-35 μm for the CH* excited radical, lower than the corresponding values calculated for the premixed flame (Fig. 6). These results show that the chemiluminescent species OH* and CH* have the potential to be used as heat release markers for non-premixed methane-air flames, since the distance between the peak observed in the heat release rate profile and their maximum mole fraction is smaller than the spatial resolution of most optical devices used to measure chemiluminescence in flames, including the Chemiluminescence Sensor. In particular, the OH* chemiluminescence maxima were found to be at the same location as the maximum heat release rate for high values of strain rate, $a = 160 - 280 \text{ s}^{-1}$. However, this beneficial property of OH* and CH* chemiluminescence may be hindered by the soot that non-premixed flames emit; therefore this finding has to be studied also experimentally.

Conclusions

In this study, a numerical evaluation of equivalence ratio measurement using OH* and CH* chemiluminescence emitted from premixed and non-premixed methane-air flames has been performed. This is very important since OH* and CH* chemiluminescence emitted from premixed natural gas and methane-air flames is used to measure the equivalence ratio, at

atmospheric pressure [7,26,59]. The counterflow geometry was implemented and laminar premixed and non-premixed methane-air flames were studied numerically using eight different mechanisms comprised different excited species sub-mechanisms and methane oxidation schemes. Results of calculations obtained at atmospheric temperature and pressure were compared with the results of absolute OH*/CH* chemiluminescent intensity ratio measurements for natural gas and methane-air flames [26]. The main findings were:

1. Peak-to-peak distances between the maximum of the chemiluminescent species OH* and CH* mole fraction profiles, HCO and [OH] x [CH₂O] and the maximum of the heat release rate have been calculated for a range of stoichiometries and strain rates: the results showed that OH* and CH* can be used as heat release rate markers, especially OH*, since the distance between the maximum of the heat release rate profile and their maximum intensity is smaller than the spatial resolution of most optical devices used to measure chemiluminescence in flames, including the Chemiluminescence Sensor used during our experiments. OH* chemiluminescence, in particular, exhibits the same performance as heat release rate marker obtained by the product of OH and CH₂O, since the difference between their peak concentrations is less than 15 μm. These numerical results agree well with results of experiments performed at laminar hydrocarbon-fuelled Bunsen flames [57], where OH* and CH* chemiluminescent intensity peaks found to coincide with heat release rate peaks measured with simultaneous OH and CH₂O PLIF.
2. The calculated peak-to-peak distances between the species mole fraction profiles and the heat release rate, found to be independent of strain rate, while the equivalence ratio had a small effect only for rich stoichiometries.
3. The sequence of the location of the calculated maximum intensities for the OH* and CH* excited radicals, is OH* followed by CH*, as one scans the flame from the reactants to the

products. The calculated distance between them agrees well with the experimental results found in the literature [2,24,58].

4. Calculated chemiluminescent intensities from OH* and CH* are highly dependent on equivalence ratio and strain rate for $\phi > 0.9$. In contrast, results from experiment showed a strain rate effect for all the range of ϕ studied. Calculated maximum mole fractions of OH* and CH* peaked at $\phi = 1.1$, while the measured intensities at $\phi = 1.0$.
5. The spatial maximum in the calculated OH* intensity correlates well with the spatial maximum in the heat release rate, as a function of ϕ and strain rate, which supports the argument that OH* chemiluminescence could be used as heat release rate marker. The same results were observed for CH* chemiluminescence, but the correlation with heat release rate was not apparent for $0.6 \leq \phi < 0.9$.
6. Comparison between the calculated and the experimentally measured OH*/CH* ratio showed good qualitative agreement between calculations and experiment for all the mechanisms studied here. More specifically:
 - a. The OH*/CH* ratio depended monotonically only on equivalence ratio, for all mechanisms studied.
 - b. There was, in general, no effect of strain rate on the calculated OH*/CH* chemiluminescent intensity ratio, for all mechanisms studied.

This agreement between experiment and numerical results confirms that this ratio can be used to measure equivalence ratio in premixed methane-air flames at atmospheric pressure. A small effect of strain rate on the calculated OH*/CH* chemiluminescent intensity ratio observed for lean values of stoichiometry was found to correlate with the use of GRI-Mech 3.0 as the methane oxidation scheme.

7. Quantitatively, there was a disagreement between the calculated and measured absolute values of the OH*/CH* intensity ratio, for all except one of the mechanisms studied in

this work. The calculated and measured values of the OH*/CH* ratio had the same order of magnitude only for mechanisms 4 - 8. The best performed mechanism was mechanism 8, which gave results less than 30% greater than our experimental data and the observed gradient of the values was equal to the experimental data for $\phi = 0.8 - 1.2$.

8. The Lindstedt *et al.* [47-49] detailed methane oxidation scheme performed better in terms of the prediction of the precursors of the excited species OH* and CH* (CH and C₂H) than GRI-Mech 3.0, for the conditions studied in this work. This was probably due to overestimation of the CH radical by GRI-Mech 3.0 as has been reported by Gibaud *et al.* [65].
9. The best performed rate constants for OH* formation were those reported by Porter *et al.* [18] and Carl *et al.* [36], which are approximately of the same magnitude. For CH* formation, the recently published rate constants of Elsamra *et al.* [45] performed slightly better than the Devriendt *et al.* [44] ones.
10. The results of calculations for strained non-premixed counterflow methane-air flames showed that the OH*/CH* intensity ratio has the potential to be used as a criterion to decide if non-premixed or premixed combustion occurs. This is very important when a chemiluminescence-based technique is used to measure the equivalence ratio of the reacting mixture of a partially premixed turbulent flames.
11. Calculations showed that OH* and CH* have the potential to be used as heat release markers for strained non-premixed methane-air flames. However, this finding should also be confirmed experimentally.

In the future a sensitivity analysis should be performed on the excited species mechanisms, in order to explain why the OH*/CH* chemiluminescent intensity ratio is unaffected by the strain rate, and is a monotonic function of the equivalence ratio.

Acknowledgments

The authors acknowledge financial support from the UK Engineering and Physical Sciences Research Council (EPSRC), Rolls-Royce plc, SIEMENS and the Commission of the European Union. Helpful discussions with Drs. G. P. Smith (SRI) and Shaun A. Carl (University of Leuven) are greatly appreciated.

References

- [1] N. Docquier, S. Candel, *Progress In Energy and Combustion Science* 28 (2002) 107-150.
- [2] J. Kojima, Y. Ikeda, T. Nakajima, *Proc. Combust. Inst.* 28 (2000) 1757-1764.
- [3] J. G. Lee, K. Kim, D. A. Santavicca, *Proc. Combust. Inst.* 28 (2000) 739–746.
- [4] H. N. Najm, O. M.Knio, P. H. Paul, P. S. Wyckoff, *Combustion Science and Technology* 140 (1998) 369-403.
- [5] H. N. Najm, P. H. Paul, C. J. Mueller, P. S. Wyckoff, *Combust. Flame* 113 (1998) 312-332.
- [6] J. G. Lee, D. A. Santavicca, *Journal of Propulsion and Power* 19 (5) (2003) 735-750.
- [7] Y. Hardalupas, M. Orain, *Combust. Flame* 139 (2004) 188-207.
- [8] P.G. Aleiferis, Y. Hardalupas, A.M.K.P. Taylor, K. Ishii, Y. Urata, *Combust. Flame* 136 (2004) 72-90.
- [9] N. Docquier, S. Candel, *Progress Energy Comb. Science* 28 (2002) 107-150.
- [10] N. Docquier, F. Lacas, S. Candel, *Proc. Combust. Inst.* 29 (2002) 139-145.
- [11] T. M. Muruganandam, B. Kim, R. Olsen, M. Patel, B. Romig, J. M. Seitzman, AIAA 2003-4490 (2003).
- [12] T. M. Muruganandam, B. -H. Kim, M. R. Morrell, V. Nori, M. Patel, B. W. Romig, J. M. Seitzman, *Proc. Combust. Inst.* 30 (2005) 1601-1609.
- [13] F. Akamatsu, T. Wakabayashi, S. Tsushima, Y. Mizutani, Y. Ikeda, N. Kawahara, T. Nakajima, *Meas. Sci. Technol.* 10 (1999) 1240-1246.
- [14] D. Dandy, S. Vosen, *Combust. Sci. and Tech.* 82 (1992) 131-150.
- [15] K.T. Walsh, M.B. Long, M.A. Tanoff, M. D. Smooke, *Proc. Combust. Inst.* 27 (1998) 615-623.

- [16] M. R. Berman, J. W. Fleming, A. B. Harvey, M. C. Lin, *Proc. Combust. Inst.* 19 (1982) 73-79.
- [17] J. Luque, J. B. Jeffries, G. P. Smith, D. R. Crosley, K. T. Walsh, M. B. Long, M. D. Smooke, *Combust. Flame* 122 (2000) 172-175.
- [18] R. P. Porter, A. H. Clark, W. E. Kaskan, W. E. Browne, *Proc. Combust. Inst.* 11 (1967) 907-917.
- [19] N. Docquier, S. Belhafaoui, F. Lacas, N. Darabiha, C. Rolon, *Proc. Combust. Inst.* 28 (2000) 1765-1774.
- [20] B. Higgins, M.Q. McQuay, F. Lacas, J. C. Rolon, N. Darabiha, S. Candel, *Fuel* 80 (2001) 67-74.
- [21] B. Higgins, M.Q. McQuay, F. Lacas, S. Candel, *Fuel* 80 (2001) 1583-1591.
- [22] C.T. Bowman, R.K. Hanson, D.F. Davidson, W.C. Gardiner, Jr., V. Lissianski, G.P. Smith, D.M. Golden, M. Frenklach, M. Goldenberg, http://www.me.berkeley.edu/gri_mech/
- [23] G. P. Smith, J. Luque, C. Park, J. B. Jeffries, D. R. Crosley, *Combust. Flame* 131 (2002) 59-69.
- [24] J. Kojima, Y. Ikeda, T. Nakajima, *Combust. Flame* 140 (2005) 34-45.
- [25] G. P. Smith, D. M. Golden, M. Frenklach, N. W. Moriarty, B. Eiteneer, M. Goldenberg, C. T. Bowman, R. K. Hanson, S. Song, W. C. Gardiner, Jr., V. V. Lissianski, Z. Qin, GRI-Mech 3.0 Web site, http://www.me.berkeley.edu/gri_mech/, 1999.
- [26] C. S. Panoutsos, *Experimental and Theoretical Study of Chemiluminescence in Premixed Flames*, Ph.D. Thesis, University of London, 2007.
- [27] A. E. Lutz, R. J. Kee, *A FORTRAN Program for Computing Opposed-Flow Diffusion Flames*, Sandia National Laboratories, Sandia Report No. SAND96-8243, 1996.

- [28] R. J. Kee, F. M. Rupley, J. A. Miller, *CHEMKIN-II: A Fortran chemical kinetics package for the analysis of gas phase chemical kinetics*, Sandia National Laboratories, Sandia Report No. SAND-89-8009, 1989.
- [29] R. J. Kee, M. E. Coltrin, and P. Glarborg. *Chemically Reacting Flow: Theory and Practice*. John Wiley, New York, 2003, p. 705.
- [30] R. J. Kee, J. A. Miller, G. H. Evans, G. Dixon-Lewis, *Proc. Combust. Inst.* 22 (1988) 1479-1494.
- [31] A. G. Gaydon, *Spectroscopy of Flames*, Chapman and Hall, London, U.K., 1957, p. 160, 196.
- [32] S. Krishnamachari, H. Broida, *J. Chem. Phys.* 34 (5) (1961) 1709-11.
- [33] C. T. Bowman, D. J. Seery, *Combust. Flame* 12 (1968) 611-614.
- [34] J. Grebe, K. H. Homann, *Berichte der Bunsen-Gesellschaft für Physikalische Chemie* 86 (1982) 581-587.
- [35] L.C. Haber, U. Vandsburger, *Combust. Sci. and Tech.* 175 (2003) 1859-1891.
- [36] S. A. Carl, M. Van Poppel, J. Peeters, *J. Phys. Chem. A* 107 (2003) 11001-11007.
- [37] G. P. Smith, C. Park, J. Luque, *Combust. Flame* 140 (2005) 385-389.
- [38] J. M. Hall, E. L. Petersen, *International Journal of Chemical Kinetics* 38 (2006) 714-724.
- [39] J. M. Hall, E. L. Petersen, AIAA 2004-4164 (2004).
- [40] M. Tamura, P.A. Berg, J.E. Harrington, J. Luque, J.B. Jeffries, G.P. Smith, D.R. Crosley, *Combust. Flame* 114 (3-4) (1998) 502-514.
- [41] G. Glass, G. Kistiakowsky, J. Michael, H. Niki, *Proc. Combust. Inst.* 10 (1965) 513-525.
- [42] R. G. Joklik, J. W. Daily, W. J. Pitz, *Proc. Combust. Inst.* 21 (1986) 895-904.
- [43] K. Devriendt, J. Peeters, *J. Phys. Chem. A* 101 (1997) 2546-2551.

- [44] K. Devriendt, H. Van Look, J. Ceursters, J. Peeters, *Chem. Phys. Lett.* 261 (1996) 450-456.
- [45] R. M. I. Elsamra, S. Vranckx, S. A. Carl, *J. Phys. Chem. A* 109 (2005) 10287-10293.
- [46] J. Luque, G. P. Smith, J. B. Jeffries, D. R. Crosley, AIAA-2001-0626 (2001).
- [47] R. P. Lindstedt, G. Skevis, *Combust. Sci. and Tech.* 125 (1997) 73-137.
- [48] R. P. Lindstedt, F. C. Lockwood, M. A. Selim, *Combust. Sci. and Tech.* 99 (1994) 253-276.
- [49] M. P. Meyer, *The application of detailed and systematically reduced chemistry to transient laminar flames*, Ph.D. Thesis, University of London, 2001.
- [50] G. P. Smith, Personal Communication (2004).
- [51] Sandia National Laboratories, TNF Workshop, 2002,
<http://www.ca.sandia.gov/TNF/chemistry.html>
- [52] V. N. Nori, J. M. Seitzman, AIAA-2007-0466 (2007).
- [53] F. N. Egolfopoulos, P. Cho, C.K. Law, *Combust. Flame* 76 (1989) 375-391.
- [54] M. D. Smooke, Y. Xu, R. M. Zurn, R. M. Lin, J. H. Frank, M. B. Long, *Proc. Combust. Inst.* 24 (1992) 813-821.
- [55] P. H. Paul, H. N. Najm, *Proc. Combust. Inst.* 27 (1998) 43-50.
- [56] S. Böckle, J. Kazenwadel, T. Kunzelmann, D.-I. Shin, C. Schulz, J. Wolfrum, *Proc. Combust. Inst.* 28 (2000) 279-286.
- [57] Y. Hardalupas, C. S. Panoutsos, A. M. K. P. Taylor, AIAA-2006-1450 (2006).
- [58] J. Kojima, Y. Ikeda, T. Nakajima, *Meas. Sci. and Tech.* 14 (2003) 1714-1724.
- [59] M. Orain, *Experiments with gas and liquid-fuelled flames*, Ph.D. Thesis, University of London, 2001.
- [60] S. L. Baughcum, R. C. Oldenborg, *A. C. S. Symp.* 249 (1984) 257-266.
- [61] S. Hwang, W. C. Gardiner, M. Frenklach, D. Hidaka *Combust. Flame* 67 (1987) 65-76.

- [62] W. E. Kaskan, *J. Chem. Phys.* 31 (1959) 944-956; M. G. Davis, W. K. McGregor, A. A. Mason, *J. Chem. Phys.* 61 (1974) 1352-1356.
- [63] K. H. Becker, H. H. Brenig, T. Tatarczyk, *Chem. Phys. Lett.* 71 (1980) 242-245.
- [64] W. L. Dimpfl, J. L. Kinsey, *Quant. Spectrosc. Radiat. Transfer* 21 (1979) 233-241.
- [65] C. Gibaud, J. A. Snyder, V. Sick, R. P. Lindstedt, *Proc. Combust. Inst.* 30 (2005) 455–463.

Appendix

Spectral calibration of the optical detection system

The spectral calibration was performed in order to correct for the differences in the optical system's responsivity at the two spectral bands studied in this work, 308.5 ± 9.0 nm for OH* and 430.5 ± 0.95 nm for CH* intensity. A 300 W Xe lamp (6258, Newport) was utilised in order to calibrate our optical chemiluminescence measurement system. The Xe lamp was chosen because of its stable, spectrally flat output in the UV and visible spectrum. The Xe lamp had been calibrated using a spectrometer (Instaspec IV CCD, Oriol) with a spectral range from 250.3926 nm to 759.9195 nm and a resolution of 0.4976 nm/pixel, and a Tungsten lamp (CL6, Bentham Instruments Ltd). More details of this calibration can be found in [26]. The measured spectral irradiance profile from the Xe lamp can be seen in Fig. 15a, and the normalised spectral irradiance profile can be seen in Fig. 15b. The profile has been normalised by the maximum measured irradiance.

Next step of the calibration was to measure the transmittance curves of the interference filters used to measure OH* and CH* chemiluminescence. These transmittance curves will be combined to find the combined transmittance curve of our optical system to the radiation emitted from the Xe calibration lamp. By measuring the spectral irradiance of the Xe lamp with and without the interference filters placed in front of the spectrometer's fiber we were able to measure the transmittance curves of the OH* and CH* filters. These data were in good agreement with the data provided from the manufacturer of the filters (Optical Coatings Japan). The combined transmission curve for the OH* and CH* interference filters, seen in Fig. 16, is derived by combining the OH* transmission curve from 250.0 – 410.0 nm with the CH* transmission curve from 410.0 – 760.0 nm. This combined transmission curve is next

multiplied with the normalised spectral irradiance curve of the Xe calibration lamp (Fig. 15b). This provides the spectral irradiance profile transmitted through the OH* and CH* interference filters to the photomultipliers (PMs) of the spectroscopic unit (Fig. 17), having in mind that both dichroic mirrors reflect the OH* and CH* bands at the same intensity, more than 95%.

In order to calculate the ratio of the integrated irradiance delivered to the OH* band and to the CH* band, we integrate the spectral irradiance profile at the bands of interest. In Fig. 18 we focus on the OH* band and we calculate the integrated irradiance from 286.6749 to 360.7557 nm. In Fig. 19 we focus on the CH* band and we calculate the integrated irradiance from 420.0553 to 440.3143 nm. The ratio of the two integrated irradiances was found to be equal to:

$$\frac{\int_{\lambda} I_{OH^*} d\lambda}{\int_{\lambda} I_{CH^*} d\lambda} = 0.3764 \quad (\text{A.1})$$

where λ is the wavelength of the light and I the spectral irradiance.

The above ratio provides the absolute value of the ratio of the spectral irradiance at the two spectral bands of interest that is delivered to our optical system from the Xe calibration lamp. By measuring the intensity ratio of OH*/CH* using our optical sensor and comparing that ratio with the above value for the calibration lamp, we can derive an *Absolute Scale Factor* that is used to correct the measured OH*/CH* chemiluminescent intensity ratio for the differences in the optical system's responsivity.

The Xe lamp and the Chemiluminescence Sensor were placed in series on an optical rail. In front of the lamp a screen and an iris were placed in order to reduce the amount of light delivered to the Chemiluminescence Sensor to prevent saturation of the PMTs. The Cassegrain-optics sensor had to be placed at a specific angle relative to the longitudinal axis of the lamp in order to align its solid angle of detection with the direction of the light emitted from the lamp. Otherwise, the sensor would not collect the direct light emitted from the lamp, but only scattered light reflected from the particles passing through the probe volume. In addition care was taken to assure that only the probe volume of the sensor was filled with light during calibration. This was achieved by aligning the probe volume at the centre of the iris and adjusting the iris to its minimum diameter [26].

The amount of light delivered to the Cassegrain optics sensors from the 300 W Xe lamp was so intense that could saturate the photomultipliers. In order to reduce the intensity of the

light, we first misaligned the reflector and defocused the condensing optics of the lamp and second we used reflective neutral density filters with transmissions of 10%, 3.2% and 1% (NT47-207; NT47-209; NT47-210, Edmund Optics). The filters were used alone and also stacked together in order to have the optimum amount of light delivered to the sensor for different values of the gain of the photomultipliers' tubes.

The results of the measured OH*/CH* chemiluminescent intensity ratio as a function of the supply voltage to the PMs (gain) of the CS, are shown in Fig. 20. It can be seen that as the gain increases the OH*/CH* ratio slightly increases, showing a nonlinear effect of the gain on the ratio. By dividing the measured OH*/CH* intensity values with the irradiance ratio of the two spectral bands delivered from the calibration lamp, we can calculate the values of the absolute scale factor needed to correct the measured OH*/CH* chemiluminescence intensity ratio for the differences in the optical system's responsivity, as a function of the gain to the PMs (Fig. 21).

Tables

Table 1: OH* and CH* chemiluminescence reaction kinetics from Walsh *et al.* [15], added to mechanism 1. $k = AT^B \exp(-E_a/RT)$, E_a [cal/mole], R [cal mole⁻¹ K⁻¹]. h is Planck constant, and ν is the wavelength of chemiluminescent emission.

	Reaction	A	B	E_a	Ref.
1	$\text{CH} + \text{O}_2 \leftrightarrow \text{OH}^* + \text{CO}$	3.25E+13	0.00	0	[15]
2	$\text{OH}^* \rightarrow \text{OH} + h\nu$	1.45E+06	0.00	0	[40]
3	$\text{OH}^* + \text{N}_2 \leftrightarrow \text{OH} + \text{N}_2$	1.08E+11	0.50	-1238	[40]
4	$\text{OH}^* + \text{O}_2 \leftrightarrow \text{OH} + \text{O}_2$	2.10E+12	0.50	-482	[40]
5	$\text{OH}^* + \text{H}_2\text{O} \leftrightarrow \text{OH} + \text{H}_2\text{O}$	5.92E+12	0.50	-861	[40]
6	$\text{OH}^* + \text{H}_2 \leftrightarrow \text{OH} + \text{H}_2$	2.950E+12	0.50	-444	[40]
7	$\text{OH}^* + \text{CO}_2 \leftrightarrow \text{OH} + \text{CO}_2$	2.750E+12	0.50	-968	[40]
8	$\text{OH}^* + \text{CO} \leftrightarrow \text{OH} + \text{CO}$	3.230E+12	0.50	-787	[40]
9	$\text{OH}^* + \text{CH}_4 \leftrightarrow \text{OH} + \text{CH}_4$	3.360E+12	0.50	-635	[40]
10	$\text{C}_2\text{H} + \text{O} \leftrightarrow \text{CH}^* + \text{CO}$	1.080E+13	0.00	0	[44]
11	$\text{C}_2\text{H} + \text{O}_2 \leftrightarrow \text{CH}^* + \text{CO}_2$	2.170E+10	0.00	0	[44]
12	$\text{CH}^* \rightarrow \text{CH} + h\nu$	1.850E+06	0.00	0	[40]
13	$\text{CH}^* + \text{N}_2 \leftrightarrow \text{CH} + \text{N}_2$	3.030E+02	3.40	-381	[40]
14	$\text{CH}^* + \text{O}_2 \leftrightarrow \text{CH} + \text{O}_2$	2.480E+06	2.14	-1720	[40]
15	$\text{CH}^* + \text{H}_2\text{O} \leftrightarrow \text{CH} + \text{H}_2\text{O}$	5.300E+13	0.00	0	[40]
16	$\text{CH}^* + \text{H}_2 \leftrightarrow \text{CH} + \text{H}_2$	1.470E+14	0.00	1361	[40]
17	$\text{CH}^* + \text{CO}_2 \leftrightarrow \text{CH} + \text{CO}_2$	2.400E-01	4.30	-1694	[40]
18	$\text{CH}^* + \text{CO} \leftrightarrow \text{CH} + \text{CO}$	2.440E+12	0.50	0	[40]
19	$\text{CH}^* + \text{CH}_4 \leftrightarrow \text{CH} + \text{CH}_4$	1.730E+13	0.00	167	[40]

Table 2: OH* and CH* chemiluminescence starting mechanism from references [23,46], added to mechanism 2. $k = AT^B \exp(-E_a/RT)$, E_a [cal/mole], R [cal mole⁻¹ K⁻¹]. h is Planck constant, and ν is the wavelength of chemiluminescent emission.

	Reaction	A	B	E_a	Ref.
1	$C_2 + H_2 \leftrightarrow C_2H + H$	4.000E+05	2.4	1000	est. (C ₂ H + H ₂) [23]
2	$CH + CH \leftrightarrow C_2 + H_2$	5.000E+12	0.00	0	est. [23]
3	$C + C + M \leftrightarrow C_2 + M$	3.000E+14	0.00	-1000	est. (2X + M) [23]
4	$C + CH \leftrightarrow C_2 + H$	5.000E+13	0.00	0	est. (O + CH) [23]
5	$O + C_2 \leftrightarrow C + CO$	5.000E+13	0.00	0	est. (O + CH) [23]
6	$C_2 + O_2 \leftrightarrow CO + CO$	9.000E+12	0.00	980	[60]
7	$CH + O_2 \leftrightarrow CO + OH^*$	6.000E+10	0.00	0	[18]
8	$C_2 + OH \leftrightarrow CO + CH^*$	1.110E+13	0.00	0	[23]
9	$C_2H + O \leftrightarrow CO + CH^*$	6.200E+12	0.00	0	[42,34,44]
10	$C_2H + O_2 \leftrightarrow CO_2 + CH^*$	4.100E+13	0.00	4500	[44,61]
11	$O + H + M \leftrightarrow OH^* + M$	3.630E+13	0.00	0	[62] reanalysed
12	$C + H + M \leftrightarrow CH^* + M$	3.630E+13	0.00	0	est. (O + H + M) [23]
13	$CH^* \rightarrow CH + h\nu$	1.860E+06	0.00	0	[63]
14	$CH^* + N_2 \leftrightarrow CH + N_2$	3.030E+02	3.40	-381	[40]
15	$CH^* + O_2 \leftrightarrow CH + O_2$	2.480E+06	2.14	-1720	[40]
16	$CH^* + H_2O \leftrightarrow CH + H_2O$	5.300E+13	0.00	0	[40]
17	$CH^* + H_2 \leftrightarrow CH + H_2$	1.470E+14	0.00	1361	[40]
18	$CH^* + CO_2 \leftrightarrow CH + CO_2$	2.410E-01	4.30	-1694	[40]
19	$CH^* + CO \leftrightarrow CH + CO$	2.440E+12	0.50	0	[40]
20	$CH^* + CH_4 \leftrightarrow CH + CH_4$	1.730E+13	0.00	167	[40]
21	$OH^* \rightarrow OH + h\nu$	1.450E+06	0.00	0	[64]
22	$OH^* + N_2 \leftrightarrow OH + N_2$	1.080E+11	0.50	-1238	[40]
23	$OH^* + O_2 \leftrightarrow OH + O_2$	2.100E+12	0.50	-482	[40]
24	$OH^* + H_2O \leftrightarrow OH + H_2O$	5.920E+12	0.50	-861	[40]
25	$OH^* + H_2 \leftrightarrow OH + H_2$	2.950E+12	0.50	-444	[40]
26	$OH^* + CO_2 \leftrightarrow OH + CO_2$	2.750E+12	0.50	-968	[40]
27	$OH^* + CO \leftrightarrow OH + CO$	3.230E+12	0.50	-787	[40]
28	$OH^* + CH_4 \leftrightarrow OH + CH_4$	3.360E+12	0.50	-635	[40]

Table 3: OH* and CH* chemiluminescence proposed optimised mechanism from references [23,46], added to mechanism 3. $k = AT^B \exp(-E_a/RT)$, E_a [cal/mole], R [cal mole⁻¹ K⁻¹]. h is Planck constant, and ν is the wavelength of chemiluminescent emission.

	Reaction	A	B	E_a	Ref.
1	$C_2 + H_2 \leftrightarrow C_2H + H$	4.000E+05	2.4	1000	est. (C ₂ H + H ₂) [23]
2	$CH + CH \leftrightarrow C_2 + H_2$	5.000E+12	0.00	0	est. [23]
3	$C + C + M \leftrightarrow C_2 + M$	3.000E+14	0.00	-1000	est. (2X + M) [23]
4	$C + CH \leftrightarrow C_2 + H$	5.000E+13	0.00	0	est. (O + CH) [23]
5	$O + C_2 \leftrightarrow C + CO$	5.000E+13	0.00	0	est. (O + CH) [23]
6	$C_2 + O_2 \leftrightarrow CO + CO$	9.000E+12	0.00	980	[60]
7	$CH + O_2 \leftrightarrow CO + OH^*$	1.800E+11	0.00	0	[23]
8	$C_2H + O \leftrightarrow CO + CH^*$	6.200E+12	0.00	0	[42,34,44]
9	$O + H + M \leftrightarrow OH^* + M$	3.630E+13	0.00	0	[62] reanalysed
10	$C + H + M \leftrightarrow CH^* + M$	3.630E+13	0.00	0	est. (O+ H + M) [23]
11	$CH^* \rightarrow CH + h\nu$	1.860E+06	0.00	0	[63]
12	$CH^* + N_2 \leftrightarrow CH + N_2$	3.030E+02	3.40	-381	[40]
13	$CH^* + O_2 \leftrightarrow CH + O_2$	2.480E+06	2.14	-1720	[40]
14	$CH^* + H_2O \leftrightarrow CH + H_2O$	5.300E+13	0.00	0	[40]
15	$CH^* + H_2 \leftrightarrow CH + H_2$	1.470E+14	0.00	1361	[40]
16	$CH^* + CO_2 \leftrightarrow CH + CO_2$	2.410E-01	4.30	-1694	[40]
17	$CH^* + CO \leftrightarrow CH + CO$	2.440E+12	0.50	0	[40]
18	$CH^* + CH_4 \leftrightarrow CH + CH_4$	1.730E+13	0.00	167	[40]
19	$OH^* \rightarrow OH + h\nu$	1.450E+06	0.00	0	[64]
20	$OH^* + N_2 \leftrightarrow OH + N_2$	1.080E+11	0.50	-1238	[40]
21	$OH^* + O_2 \leftrightarrow OH + O_2$	2.100E+12	0.50	-482	[40]
22	$OH^* + H_2O \leftrightarrow OH + H_2O$	5.920E+12	0.50	-861	[40]
23	$OH^* + H_2 \leftrightarrow OH + H_2$	2.950E+12	0.50	-444	[40]
24	$OH^* + CO_2 \leftrightarrow OH + CO_2$	2.750E+12	0.50	-968	[40]
25	$OH^* + CO \leftrightarrow OH + CO$	3.230E+12	0.50	-787	[40]
26	$OH^* + CH_4 \leftrightarrow OH + CH_4$	3.360E+12	0.50	-635	[40]

Table 4: OH* and CH* chemiluminescence elementary reactions from Luque *et al.* [17], added to mechanisms 4 & 5. $k = AT^B \exp(-E_a/RT)$, E_a [cal/mole], R [cal mole⁻¹ K⁻¹]. h is Planck constant, and ν is the wavelength of chemiluminescent emission.

	Reaction	A	B	E_a	Ref.
1	$\text{CH} + \text{O}_2 \leftrightarrow \text{OH}^* + \text{CO}$	6.000E+10	0.00	0	[18]
2	$\text{OH}^* \rightarrow \text{OH} + h\nu$	1.450E+06	0.00	0	[40]
3	$\text{OH}^* + \text{N}_2 \leftrightarrow \text{OH} + \text{N}_2$	1.080E+11	0.50	-1238	[40]
4	$\text{OH}^* + \text{O}_2 \leftrightarrow \text{OH} + \text{O}_2$	2.100E+12	0.50	-482	[40]
5	$\text{OH}^* + \text{H}_2\text{O} \leftrightarrow \text{OH} + \text{H}_2\text{O}$	5.920E+12	0.50	-861	[40]
6	$\text{OH}^* + \text{H}_2 \leftrightarrow \text{OH} + \text{H}_2$	2.950E+12	0.50	-444	[40]
7	$\text{OH}^* + \text{CO}_2 \leftrightarrow \text{OH} + \text{CO}_2$	2.750E+12	0.50	-968	[40]
8	$\text{OH}^* + \text{CO} \leftrightarrow \text{OH} + \text{CO}$	3.230E+12	0.50	-787	[40]
9	$\text{OH}^* + \text{CH}_4 \leftrightarrow \text{OH} + \text{CH}_4$	3.360E+12	0.50	-635	[40]
10	$\text{C}_2\text{H} + \text{O} \leftrightarrow \text{CH}^* + \text{CO}$	1.080E+13	0.00	0	[44]
11	$\text{C}_2\text{H} + \text{O}_2 \leftrightarrow \text{CH}^* + \text{CO}_2$	2.170E+10	0.00	0	[44]
12	$\text{CH}^* \rightarrow \text{CH} + h\nu$	1.850E+06	0.00	0	[40]
13	$\text{CH}^* + \text{N}_2 \leftrightarrow \text{CH} + \text{N}_2$	3.030E+02	3.40	-381	[40]
14	$\text{CH}^* + \text{O}_2 \leftrightarrow \text{CH} + \text{O}_2$	2.480E+06	2.14	-1720	[40]
15	$\text{CH}^* + \text{H}_2\text{O} \leftrightarrow \text{CH} + \text{H}_2\text{O}$	5.300E+13	0.00	0	[40]
16	$\text{CH}^* + \text{H}_2 \leftrightarrow \text{CH} + \text{H}_2$	1.470E+14	0.00	1361	[40]
17	$\text{CH}^* + \text{CO}_2 \leftrightarrow \text{CH} + \text{CO}_2$	2.400E-01	4.30	-1694	[40]
18	$\text{CH}^* + \text{CO} \leftrightarrow \text{CH} + \text{CO}$	2.440E+12	0.50	0	[40]
19	$\text{CH}^* + \text{CH}_4 \leftrightarrow \text{CH} + \text{CH}_4$	1.730E+13	0.00	167	[40]

Table 5: OH* and CH* chemiluminescence reaction kinetics of mechanism 6, proposed in this work. $k = AT^B \exp(-E_a/RT)$, E_a [cal/mole], R [cal mole⁻¹ K⁻¹]. h is Planck constant, and ν is the wavelength of chemiluminescent emission.

	Reaction	A	B	E_a	Ref.
1	$\text{CH} + \text{O}_2 \leftrightarrow \text{OH}^* + \text{CO}$	6.00E+10	0.00	0	[18]
2	$\text{OH}^* \rightarrow \text{OH} + h\nu$	1.45E+06	0.00	0	[40]
3	$\text{OH}^* + \text{N}_2 \leftrightarrow \text{OH} + \text{N}_2$	1.08E+11	0.50	-1238	[40]
4	$\text{OH}^* + \text{O}_2 \leftrightarrow \text{OH} + \text{O}_2$	2.10E+12	0.50	-482	[40]
5	$\text{OH}^* + \text{H}_2\text{O} \leftrightarrow \text{OH} + \text{H}_2\text{O}$	5.92E+12	0.50	-861	[40]
6	$\text{OH}^* + \text{H}_2 \leftrightarrow \text{OH} + \text{H}_2$	2.95E+12	0.50	-444	[40]
7	$\text{OH}^* + \text{CO}_2 \leftrightarrow \text{OH} + \text{CO}_2$	2.75E+12	0.50	-968	[40]
8	$\text{OH}^* + \text{CO} \leftrightarrow \text{OH} + \text{CO}$	3.23E+12	0.50	-787	[40]
9	$\text{OH}^* + \text{CH}_4 \leftrightarrow \text{OH} + \text{CH}_4$	3.36E+12	0.50	-635	[40]
10	$\text{C}_2\text{H} + \text{O} \leftrightarrow \text{CH}^* + \text{CO}$	6.02E+12	0.00	457	[45]
11	$\text{C}_2\text{H} + \text{O}_2 \leftrightarrow \text{CH}^* + \text{CO}_2$	6.02E-04	4.40	-2285	[45]
12	$\text{CH}^* \rightarrow \text{CH} + h\nu$	1.85E+06	0.00	0	[40]
13	$\text{CH}^* + \text{N}_2 \leftrightarrow \text{CH} + \text{N}_2$	3.03E+02	3.40	-381	[40]
14	$\text{CH}^* + \text{O}_2 \leftrightarrow \text{CH} + \text{O}_2$	2.48E+06	2.14	-1720	[40]
15	$\text{CH}^* + \text{H}_2\text{O} \leftrightarrow \text{CH} + \text{H}_2\text{O}$	5.30E+13	0.00	0	[40]
16	$\text{CH}^* + \text{H}_2 \leftrightarrow \text{CH} + \text{H}_2$	1.47E+14	0.00	1361	[40]
17	$\text{CH}^* + \text{CO}_2 \leftrightarrow \text{CH} + \text{CO}_2$	2.40E-01	4.30	-1694	[40]
18	$\text{CH}^* + \text{CO} \leftrightarrow \text{CH} + \text{CO}$	2.44E+12	0.50	0	[40]
19	$\text{CH}^* + \text{CH}_4 \leftrightarrow \text{CH} + \text{CH}_4$	1.73E+13	0.00	167	[40]

Table 6: OH* and CH* chemiluminescence reaction kinetics of mechanism 7, proposed in this work. $k = AT^B \exp(-E_a/RT)$, E_a [cal/mole], R [cal mole⁻¹ K⁻¹]. h is Planck constant, and ν is the wavelength of chemiluminescent emission.

	Reaction	A	B	E_a	Ref.
1	$\text{CH} + \text{O}_2 \leftrightarrow \text{OH}^* + \text{CO}$	4.82E+10	0.00	167	[36]
2	$\text{OH}^* \rightarrow \text{OH} + h\nu$	1.45E+06	0.00	0	[40]
3	$\text{OH}^* + \text{N}_2 \leftrightarrow \text{OH} + \text{N}_2$	1.08E+11	0.50	-1238	[40]
4	$\text{OH}^* + \text{O}_2 \leftrightarrow \text{OH} + \text{O}_2$	2.10E+12	0.50	-482	[40]
5	$\text{OH}^* + \text{H}_2\text{O} \leftrightarrow \text{OH} + \text{H}_2\text{O}$	5.92E+12	0.50	-861	[40]
6	$\text{OH}^* + \text{H}_2 \leftrightarrow \text{OH} + \text{H}_2$	2.95E+12	0.50	-444	[40]
7	$\text{OH}^* + \text{CO}_2 \leftrightarrow \text{OH} + \text{CO}_2$	2.75E+12	0.50	-968	[40]
8	$\text{OH}^* + \text{CO} \leftrightarrow \text{OH} + \text{CO}$	3.23E+12	0.50	-787	[40]
9	$\text{OH}^* + \text{CH}_4 \leftrightarrow \text{OH} + \text{CH}_4$	3.36E+12	0.50	-635	[40]
10	$\text{C}_2\text{H} + \text{O} \leftrightarrow \text{CH}^* + \text{CO}$	6.02E+12	0.00	457	[45]
11	$\text{C}_2\text{H} + \text{O}_2 \leftrightarrow \text{CH}^* + \text{CO}_2$	6.02E-04	4.40	-2285	[45]
12	$\text{CH}^* \rightarrow \text{CH} + h\nu$	1.85E+06	0.00	0	[40]
13	$\text{CH}^* + \text{N}_2 \leftrightarrow \text{CH} + \text{N}_2$	3.03E+02	3.40	-381	[40]
14	$\text{CH}^* + \text{O}_2 \leftrightarrow \text{CH} + \text{O}_2$	2.48E+06	2.14	-1720	[40]
15	$\text{CH}^* + \text{H}_2\text{O} \leftrightarrow \text{CH} + \text{H}_2\text{O}$	5.30E+13	0.00	0	[40]
16	$\text{CH}^* + \text{H}_2 \leftrightarrow \text{CH} + \text{H}_2$	1.47E+14	0.00	1361	[40]
17	$\text{CH}^* + \text{CO}_2 \leftrightarrow \text{CH} + \text{CO}_2$	2.40E-01	4.30	-1694	[40]
18	$\text{CH}^* + \text{CO} \leftrightarrow \text{CH} + \text{CO}$	2.44E+12	0.50	0	[40]
19	$\text{CH}^* + \text{CH}_4 \leftrightarrow \text{CH} + \text{CH}_4$	1.73E+13	0.00	167	[40]

Table 7: Characteristics of the different mechanisms studied in this work.

Methane Oxidation		
Mechanism	Scheme	Excited Species Sub-mechanism/Rate constants
1	GRI-Mech 2.11 [22]	Walsh <i>et al.</i> [15]
2	GRI-Mech 3.0 [25]	Starting mechanism of Smith <i>et al.</i> [23] & Luque <i>et al.</i> [46]
3	GRI-Mech 3.0 [25]	Proposed optimised mechanism of Smith <i>et al.</i> [23] & Luque <i>et al.</i> [46]
4	GRI-Mech 3.0 [25]	Luque <i>et al.</i> [17]
5	Lindstedt <i>et al.</i> [47-49]	Luque <i>et al.</i> [17]
6*	GRI-Mech 3.0 [25]	OH* rate constant from Porter <i>et al.</i> [18] CH* rate constants from Elsamra <i>et al.</i> [45] Collisional quenching data from Tamura <i>et al.</i> [40]
7*	GRI-Mech 3.0 [25]	OH* rate constant from Carl <i>et al.</i> [36] CH* rate constants from Elsamra <i>et al.</i> [45] Collisional quenching data from Tamura <i>et al.</i> [40]
8*	Lindstedt <i>et al.</i> [47-49]	OH* rate constant from Carl <i>et al.</i> [36] CH* rate constants from Elsamra <i>et al.</i> [45] Collisional quenching data from Tamura <i>et al.</i> [40]

* Excited species sub-mechanism proposed in this work.

List of Captions for the Figures

Fig. 1. Schematic representation of the premixed counterflow flames configuration.

Fig. 2. Comparison of calculated laminar flame speed S_u with experiment [53], using the unmodified GRI-Mech 3.0 and mechanism 4.

Fig. 3. Effect of the addition of the OH^* and CH^* reaction kinetics on a) temperature, Heat Release Rate (HRR) and the CH_4 , O_2 normalised mole fractions, b) CH , C_2H and O normalised mole fractions, for a $\phi = 0.70$ and $a = 80 \text{ s}^{-1}$ counterflow premixed CH_4 -Air flame, using GRI-Mech 3.0 (solid line) and mechanism 4 (dotted line). The graphs are rescaled to show only one of the flames. The flow is in the direction of increasing values of X . The species mole fractions and the HRR have been normalised by their maximum values. The dotted line is overlapped by the solid line.

Fig. 4. Major, minor, chemiluminescent species profiles and temperature for a $\phi = 0.70$ and $a = 320 \text{ s}^{-1}$ counterflow premixed CH_4 -Air flame. The dashed line represents the temperature profile. Mechanism 4 was used for the calculations.

Fig. 5. OH^* , CH^* , HCO , $[\text{OH}]_x[\text{CH}_2\text{O}]$, OH , CH_2O mole fraction profiles and heat release rate for a $\phi = 0.70$ and $a = 320 \text{ s}^{-1}$ counterflow premixed CH_4 -Air flame. The graph is rescaled relative to Fig. 4 to show only one of the flames. The flow is from the lower jet towards increasing values of X . Mechanism 4 used for the calculations. The profiles have been rescaled to fit the same graph: $\text{OH}^* \times 1$, $\text{CH}^* \times 10$, $\text{HCO} \times 10^{-6}$, $[\text{OH}]_x[\text{CH}_2\text{O}] \times 3 \times 10^{-5}$, $\text{OH} \times 5 \times 10^{-9}$, $\text{CH}_2\text{O} \times 2.5 \times 10^{-8}$.

Fig. 6. a) Calculated peak-to-peak distances between heat release rate and HCO , $\text{OH} \times \text{CH}_2\text{O}$, OH^* and CH^* , as a function of equivalence ratio and having the strain rate as a parameter, b) Histograms of the calculated peak-to-peak distances. Results presented have been obtained using mechanism 4.

Fig. 7. Calculated peak-to-peak distances between heat release rate and HCO, OH x CH₂O, OH* and CH*, as a function of a) strain rate, and b) equivalence ratio. Results presented have been obtained using mechanism 4.

Fig. 8. a) Maximum calculated heat release rate and normalized OH* chemiluminescent intensity as a function of equivalence ratio and having the strain rate as a parameter for premixed methane-air flames. The lines represent the chemiluminescent intensity and the symbols the heat release rate.

b) Measured (solid symbols) and calculated (lines with symbols) maximum OH* chemiluminescent intensity as a function of equivalence ratio and having the strain rate as a parameter for premixed natural gas-air flames. Values have been normalised by the maximum overall intensity. Mechanism 4 was used for the calculations. Experimental data for natural gas taken from [26].

Fig. 9. a) Maximum calculated heat release rate and normalized CH* chemiluminescent intensity as a function of equivalence ratio and having the strain rate as a parameter for premixed methane-air flames. The lines represent the chemiluminescent intensity and the symbols the heat release rate.

b) Measured (solid symbols) and calculated (lines with symbols) maximum CH* chemiluminescent intensity as a function of equivalence ratio and having the strain rate as a parameter for premixed natural gas-air flames. Values have been normalised by the maximum overall intensity. Mechanism 4 was used for the calculations. Experimental data for natural gas taken from [26].

Fig. 10. Absolute measured OH*/CH* chemiluminescent intensity ratio as a function of equivalence ratio, with the strain rate as a parameter, for premixed counterflow natural gas-air flame [26].

Fig. 11. Calculated OH*/CH* chemiluminescent intensity ratio as a function of equivalence ratio, with the strain rate as a parameter, using: a) Mechanism 1, b) Mechanism 2, c) Mechanism 3, d) Mechanism 4, e) Mechanism 5, f) Mechanism 6 and g) Mechanism 7.

Fig. 12. Calculated OH*/CH* chemiluminescent intensity ratio as a function of equivalence ratio, with the strain rate as a parameter, using mechanism 8. The results are compared with experimental data from premixed counterflow methane-air flames obtained for only one value of strain rate ($a = 240 \text{ s}^{-1}$) [26].

Fig. 13. Maximum calculated OH* and CH* chemiluminescent intensity and OH*/CH* ratio as a function of strain rate, for a non-premixed counterflow methane-air flame ($T = 300 \text{ K}$). Excited species mechanism 4 was used for the calculations.

Fig. 14. Calculated OH*/CH* chemiluminescent intensity ratio as a function of equivalence ratio, with the strain rate as a parameter, for a premixed and a non-premixed counterflow methane-air flame. $T = 300 \text{ K}$. Excited species mechanism 4 used for the calculations. Data for the premixed flame are the same with the ones shown in Fig. 11d.

Fig. 15. a) Measured spectral irradiance profile of the 300W Xe lamp, and b) normalised profile.

Fig. 16. Combined OH* and CH* interference filters transmission curve.

Fig. 17. Spectral irradiance transmitted through the OH* and CH* filters to the detectors (PMTs).

Fig. 18. Power integral transmitted through the OH* interference filter.

Fig. 19. Power integral transmitted through the CH* interference filter.

Fig. 20. Measured OH*/CH* chemiluminescent intensity ratio acquired from the Xe calibration lamp, as a function of the supply voltage to the detectors (PMTs). Line shows the polynomial fit to the measured data.

Fig. 21. Absolute scale factor used to convert measured OH*/CH* chemiluminescent intensity ratio to corrected values, as a function of the supply voltage to the detectors (PMTs). Line shows the polynomial fit to the measured data.

Figures

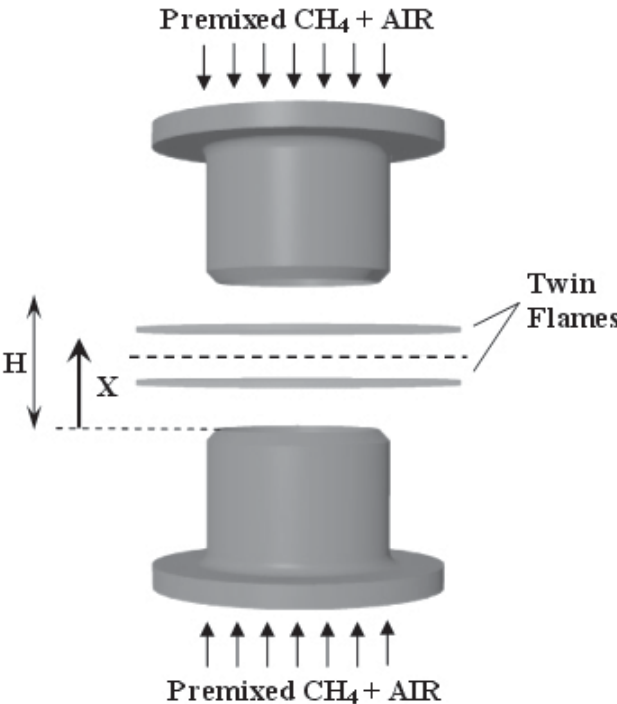


Fig. 1. Schematic representation of the premixed counterflow flames configuration.

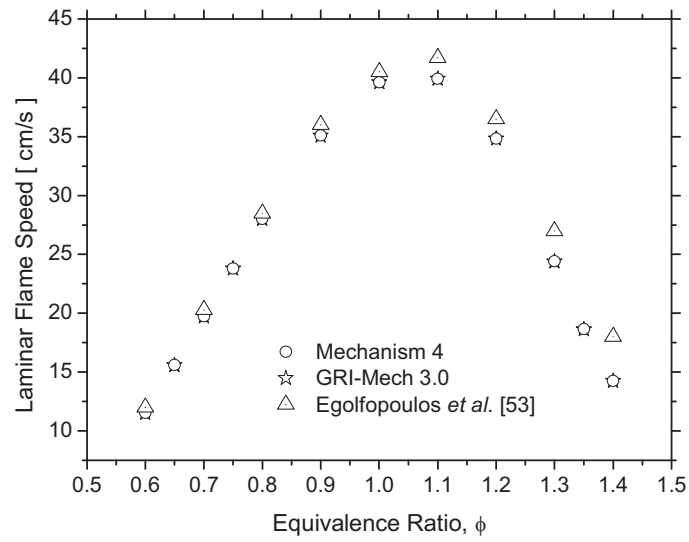
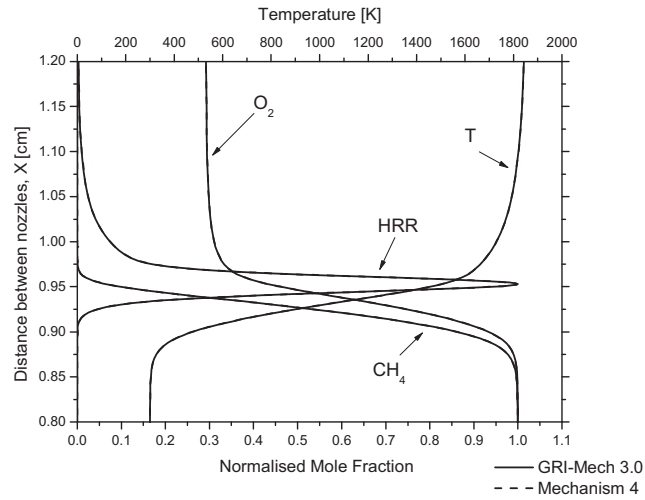
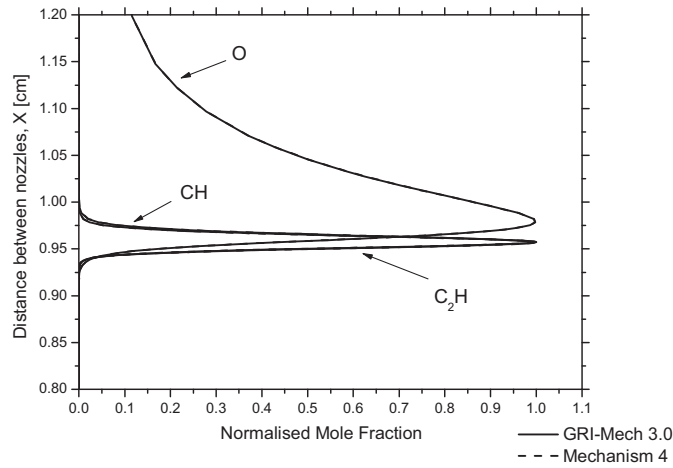


Fig. 2. Comparison of calculated laminar flame speed S_u with experiment [53], using the unmodified GRI-Mech 3.0 and mechanism 4.



a)



b)

Fig. 3. Effect of the addition of the OH^* and CH^* reaction kinetics on a) temperature, Heat Release Rate (HRR) and the CH_4 , O_2 normalised mole fractions, b) CH , C_2H and O normalised mole fractions, for a $\phi = 0.70$ and $a = 80 \text{ s}^{-1}$ counterflow premixed CH_4 -Air flame, using GRI-Mech 3.0 (solid line) and mechanism 4 (dotted line). The graphs are rescaled to show only one of the flames. The flow is in the direction of increasing values of X . The species mole fractions and the HRR have been normalised by their maximum values. The dotted line is overlapped by the solid line.

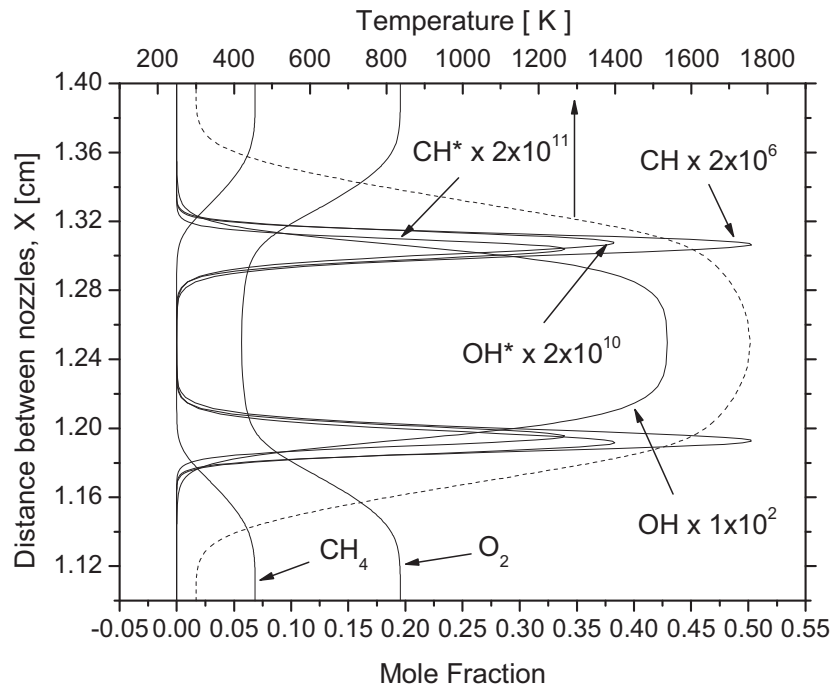


Fig. 4. Major, minor, chemiluminescent species profiles and temperature for a $\phi = 0.70$ and $a = 320 \text{ s}^{-1}$ counterflow premixed CH_4 -Air flame. The dashed line represents the temperature profile. Mechanism 4 was used for the calculations.

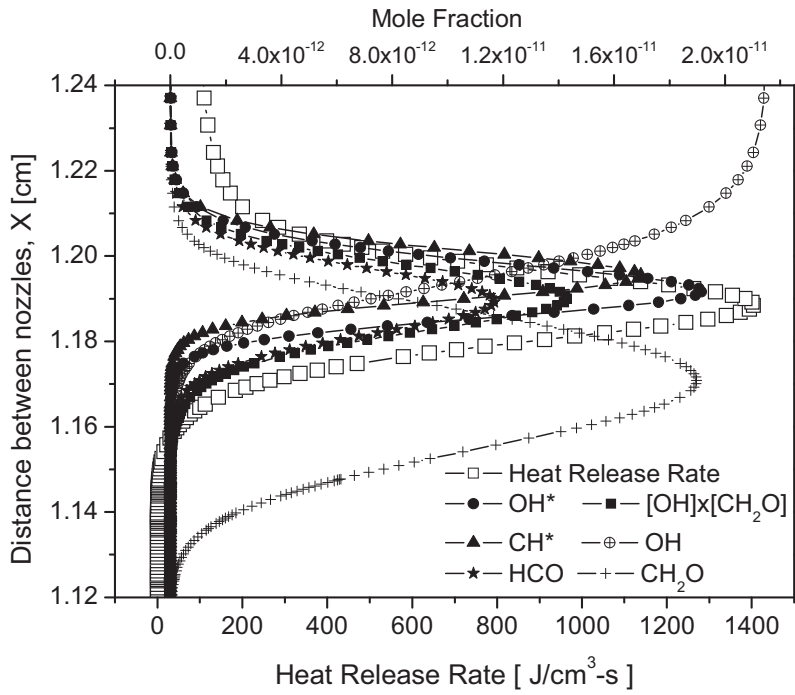


Fig. 5. OH^* , CH^* , HCO , $[\text{OH}]\times[\text{CH}_2\text{O}]$, OH , CH_2O mole fraction profiles and heat release rate for a $\phi = 0.70$ and $a = 320 \text{ s}^{-1}$ counterflow premixed CH_4 -Air flame. The graph is rescaled relative to Fig. 4 to show only one of the flames. The flow is from the lower jet towards increasing values of X . Mechanism 4 used for the calculations. The profiles have been rescaled to fit the same graph: $\text{OH}^* \times 1$, $\text{CH}^* \times 10$, $\text{HCO} \times 10^{-6}$, $[\text{OH}]\times[\text{CH}_2\text{O}] \times 3 \times 10^{-5}$, $\text{OH} \times 5 \times 10^{-9}$, $\text{CH}_2\text{O} \times 2.5 \times 10^{-8}$.

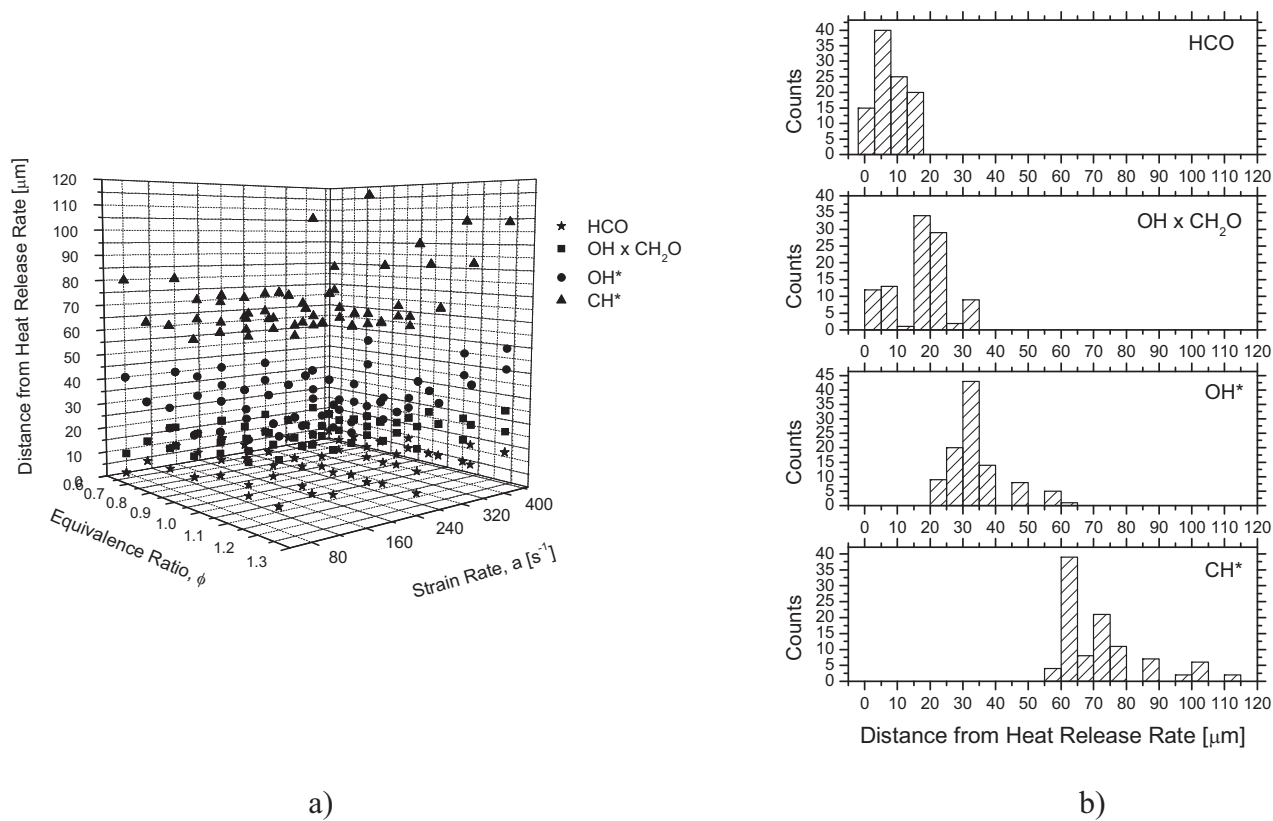
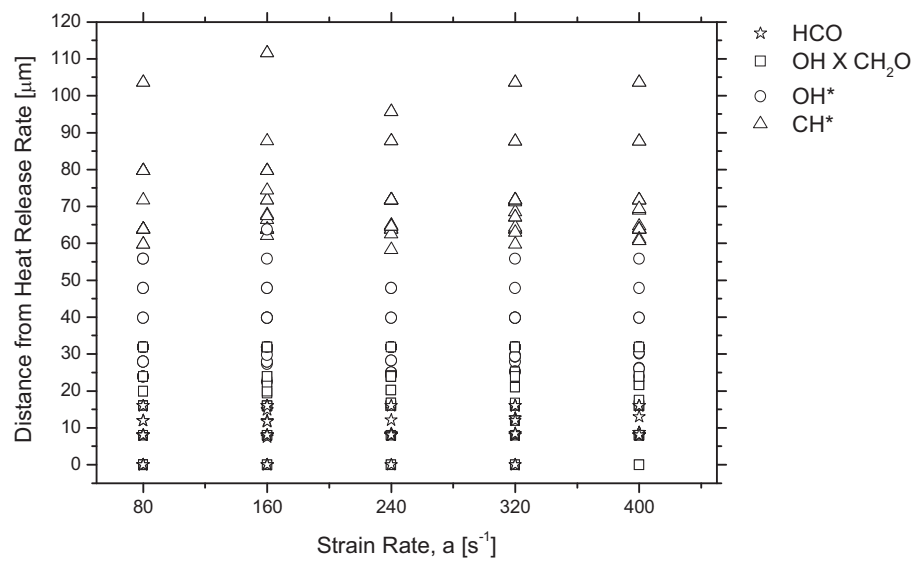
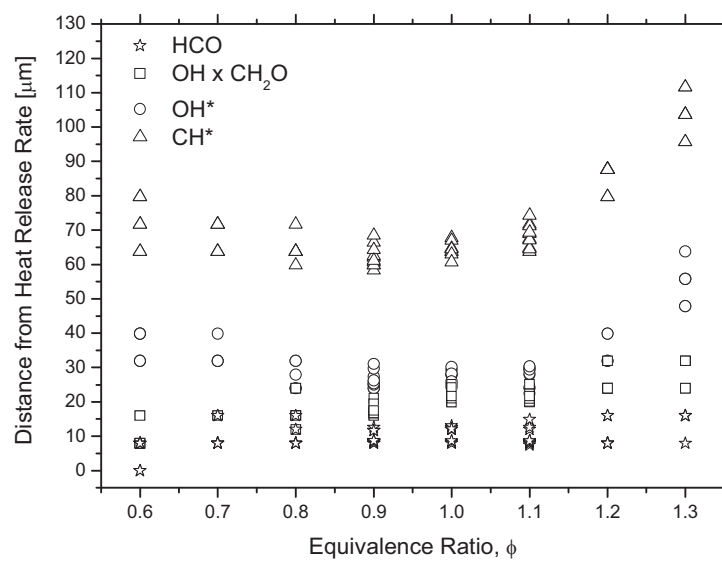


Fig. 6. a) Calculated peak-to-peak distances between heat release rate and HCO, $\text{OH} \times \text{CH}_2\text{O}$, OH^* and CH^* , as a function of equivalence ratio and having the strain rate as a parameter, b) Histograms of the calculated peak-to-peak distances. Results presented have been obtained using mechanism 4.

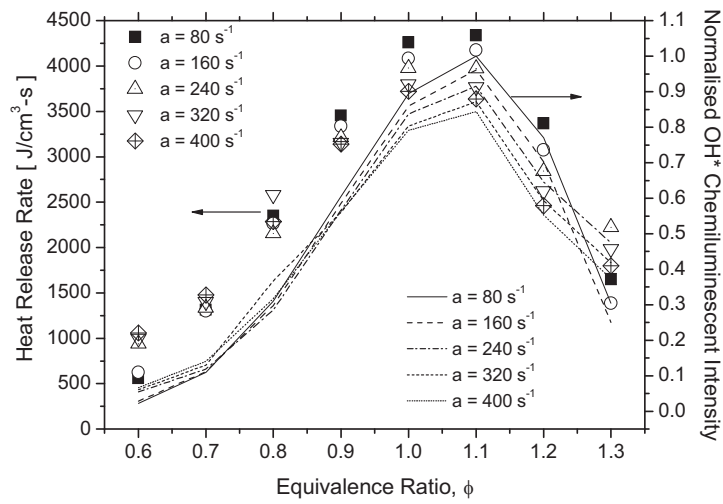


a)

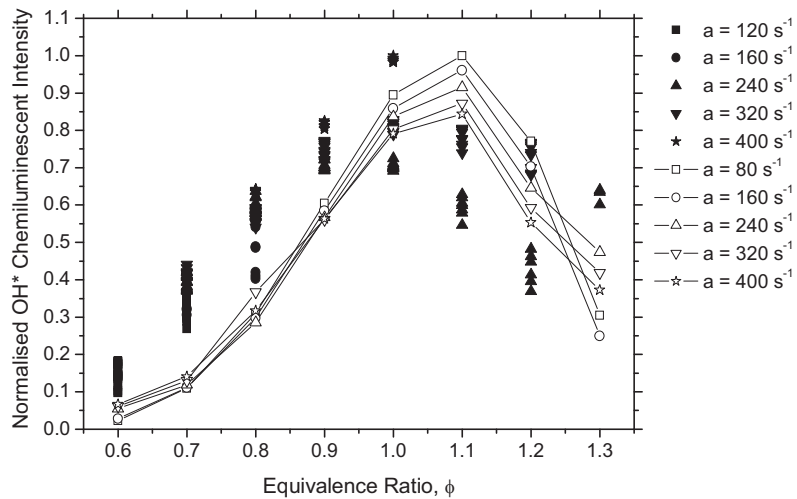


b)

Fig. 7. Calculated peak-to-peak distances between heat release rate and HCO, $\text{OH} \times \text{CH}_2\text{O}$, OH^* and CH^* , as a function of a) strain rate, and b) equivalence ratio. Results presented have been obtained using mechanism 4.



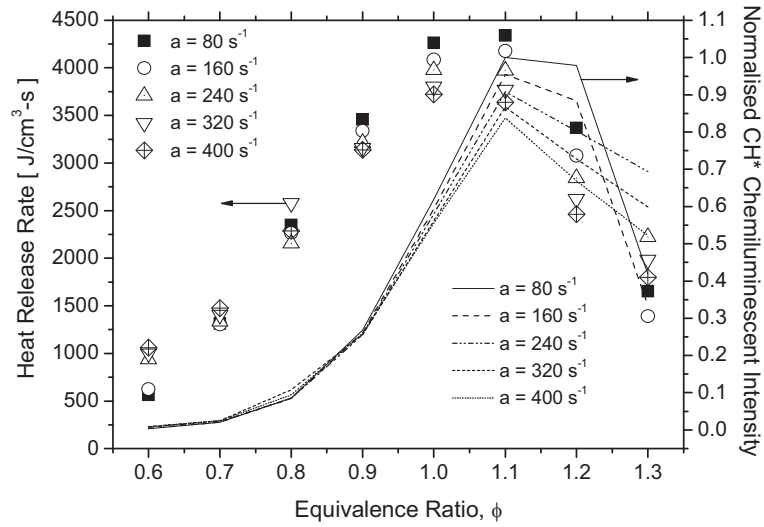
a)



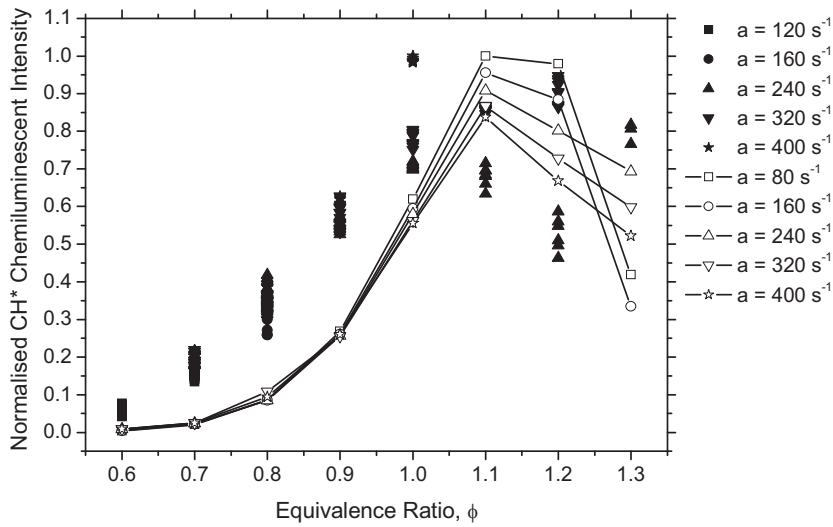
b)

Fig. 8. a) Maximum calculated heat release rate and normalized OH^* chemiluminescent intensity as a function of equivalence ratio and having the strain rate as a parameter for premixed methane-air flames. The lines represent the chemiluminescent intensity and the symbols the heat release rate.

b) Measured (solid symbols) and calculated (lines with symbols) maximum OH^* chemiluminescent intensity as a function of equivalence ratio and having the strain rate as a parameter for premixed natural gas-air flames. Values have been normalised by the maximum overall intensity. Mechanism 4 was used for the calculations. Experimental data for natural gas taken from [26].



a)



b)

Fig. 9. a) Maximum calculated heat release rate and normalized CH* chemiluminescent intensity as a function of equivalence ratio and having the strain rate as a parameter for premixed methane-air flames. The lines represent the chemiluminescent intensity and the symbols the heat release rate.

b) Measured (solid symbols) and calculated (lines with symbols) maximum CH* chemiluminescent intensity as a function of equivalence ratio and having the strain rate as a parameter for premixed natural gas-air flames. Values have been normalised by the maximum overall intensity. Mechanism 4 was used for the calculations. Experimental data for natural gas taken from [26].

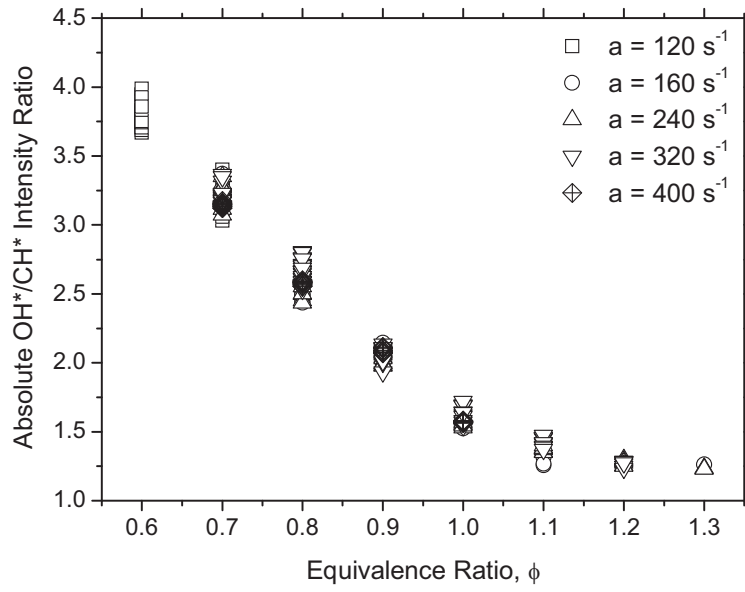
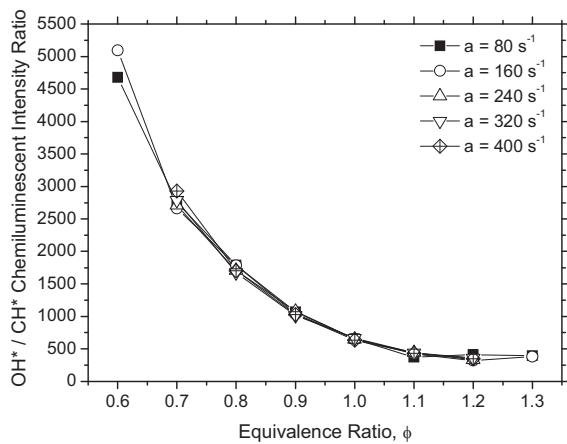
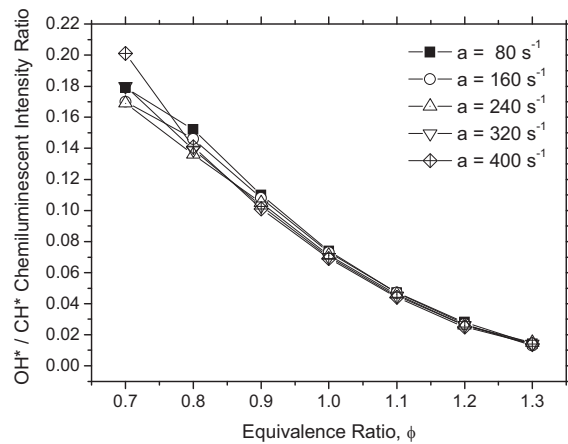


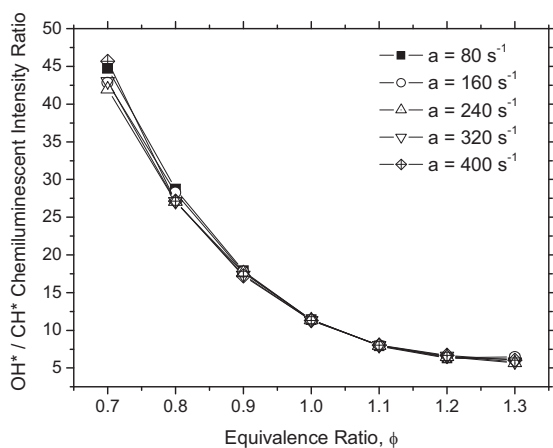
Fig. 10. Absolute measured OH*/CH* chemiluminescent intensity ratio as a function of equivalence ratio, with the strain rate as a parameter, for premixed counterflow natural gas-air flame [26].



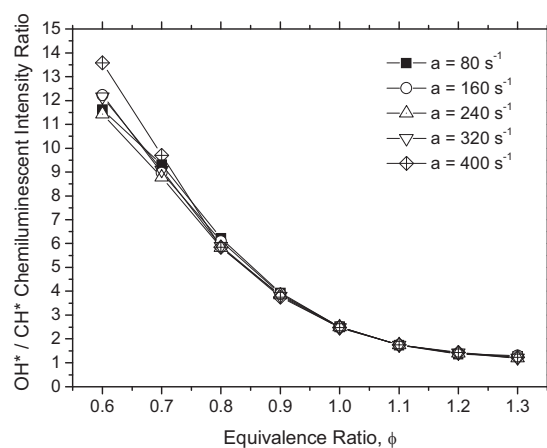
a)



b)

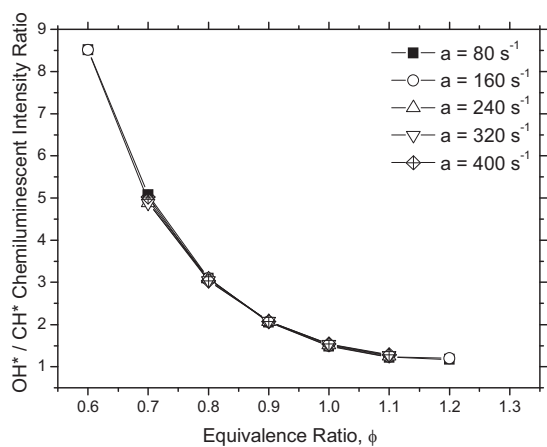


c)

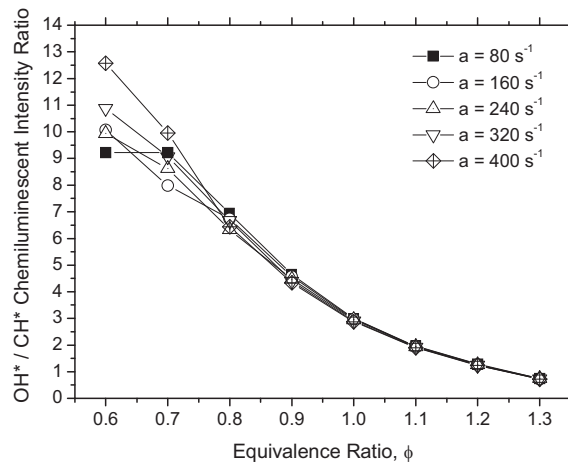


d)

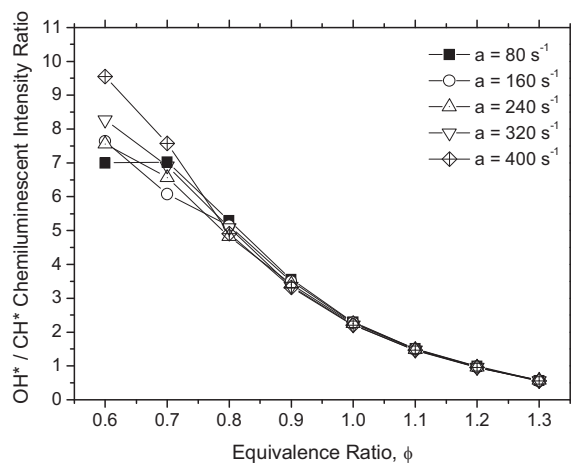
Fig. 11. Calculated OH*/CH* chemiluminescent intensity ratio as a function of equivalence ratio, with the strain rate as a parameter, using: a) Mechanism 1, b) Mechanism 2, c) Mechanism 3, d) Mechanism 4.



e)



f)



g)

Fig. 11 (continued). Calculated OH^*/CH^* chemiluminescent intensity ratio as a function of equivalence ratio, with the strain rate as a parameter, using: e) Mechanism 5, f) Mechanism 6, and g) Mechanism 7.

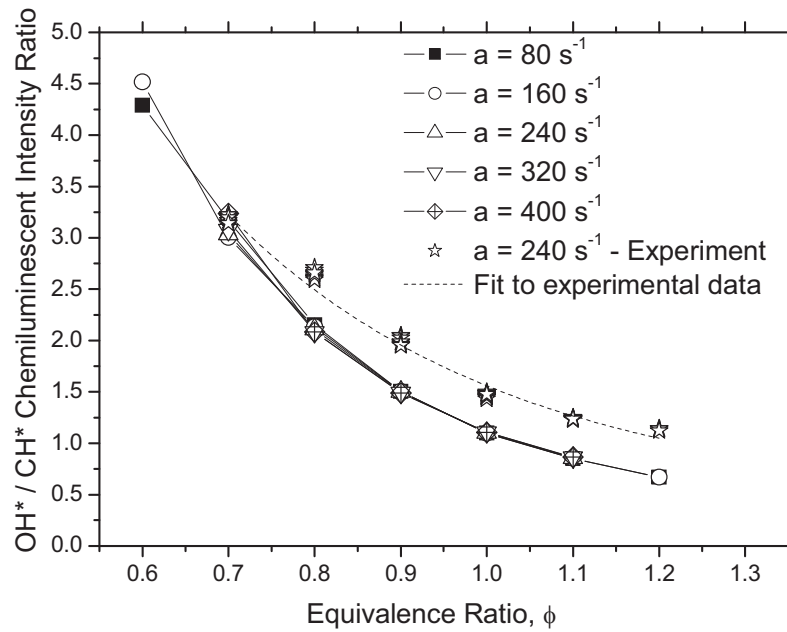


Fig. 12. Calculated OH*/CH* chemiluminescent intensity ratio as a function of equivalence ratio, with the strain rate as a parameter, using mechanism 8. The results are compared with experimental data from premixed counterflow methane-air flames obtained for only one value of strain rate ($a = 240 \text{ s}^{-1}$) [26].

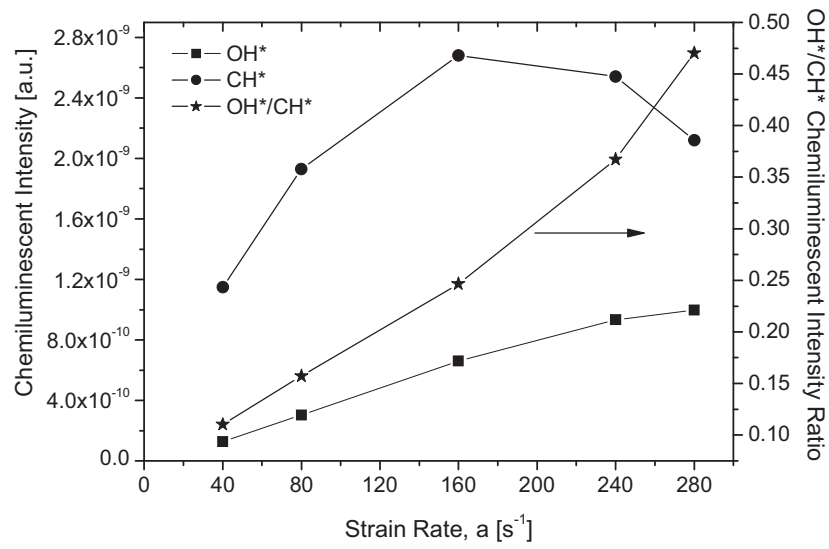


Fig. 13. Maximum calculated OH* and CH* chemiluminescent intensity and OH*/CH* ratio as a function of strain rate, for a non-premixed counterflow methane-air flame ($T = 300$ K). Excited species mechanism 4 was used for the calculations.

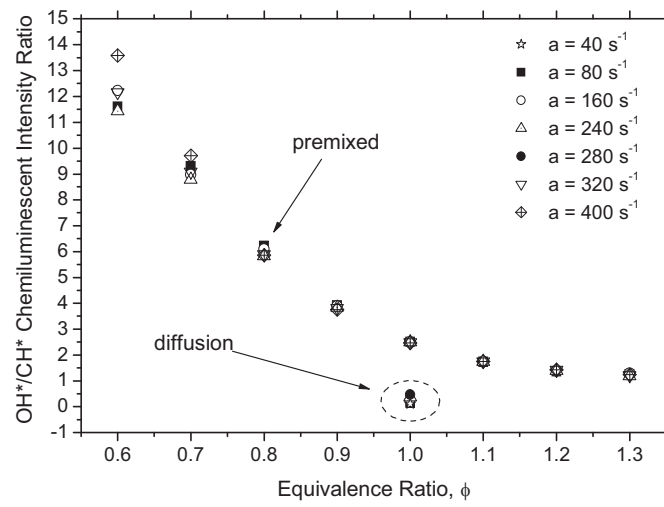
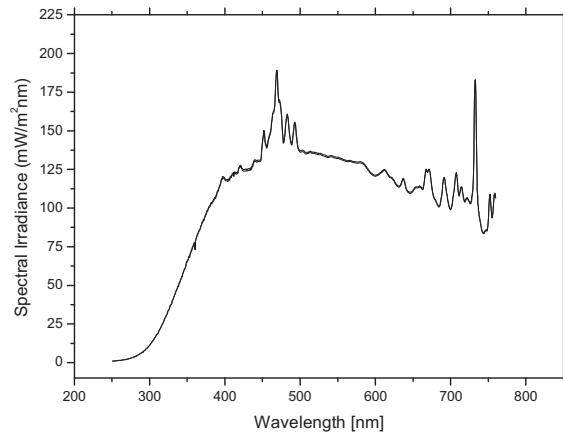
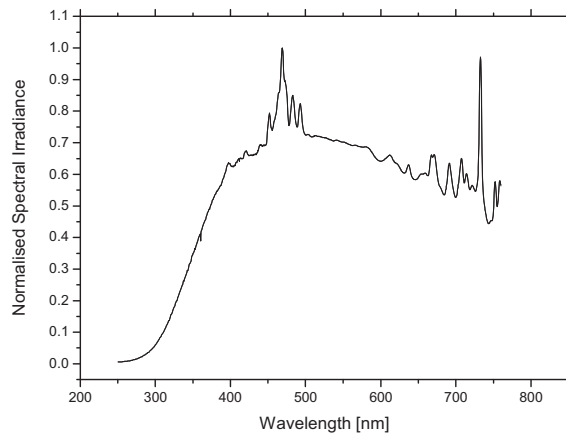


Fig. 14. Calculated OH*/CH* chemiluminescent intensity ratio as a function of equivalence ratio, with the strain rate as a parameter, for a premixed and a non-premixed counterflow methane-air flame. $T = 300 \text{ K}$. Excited species mechanism 4 used for the calculations. Data for the premixed flame are the same with the ones shown in Fig. 11d.



a



b

Fig. 15. a) Measured spectral irradiance profile of the 300W Xe lamp, and b) normalised profile.

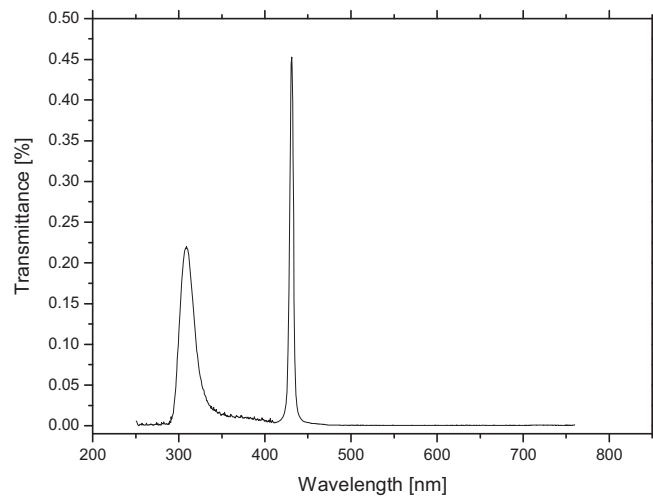


Fig. 16. Combined OH* and CH* interference filters transmission curve.

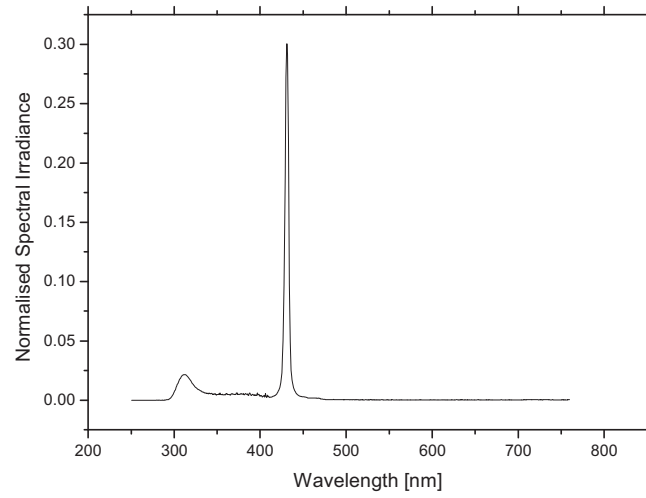


Fig. 17. Spectral irradiance transmitted through the OH* and CH* filters to the detectors (PMTs).

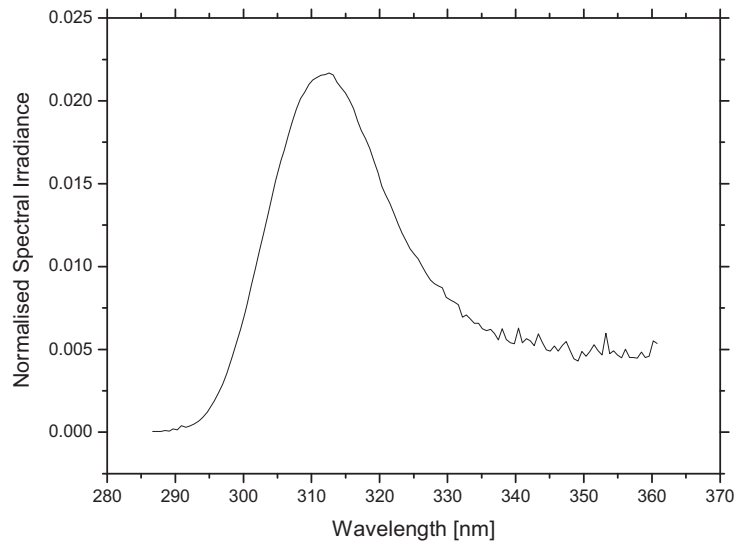


Fig. 18. Power integral transmitted through the OH* interference filter.

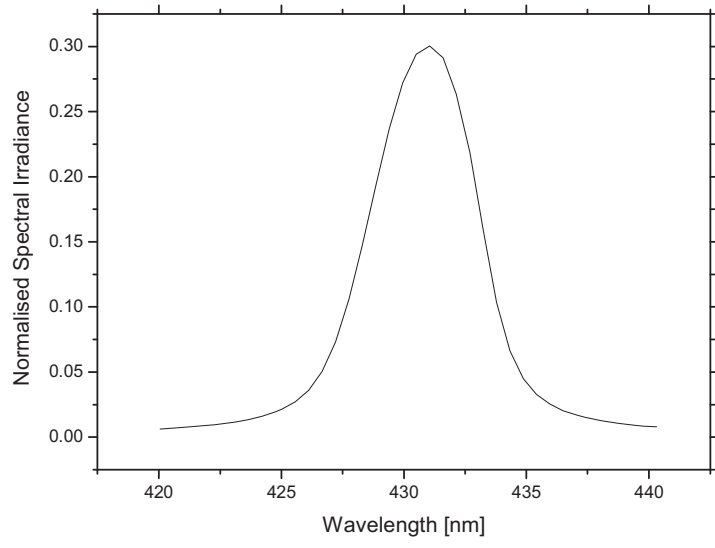


Fig. 19. Power integral transmitted through the CH* interference filter.

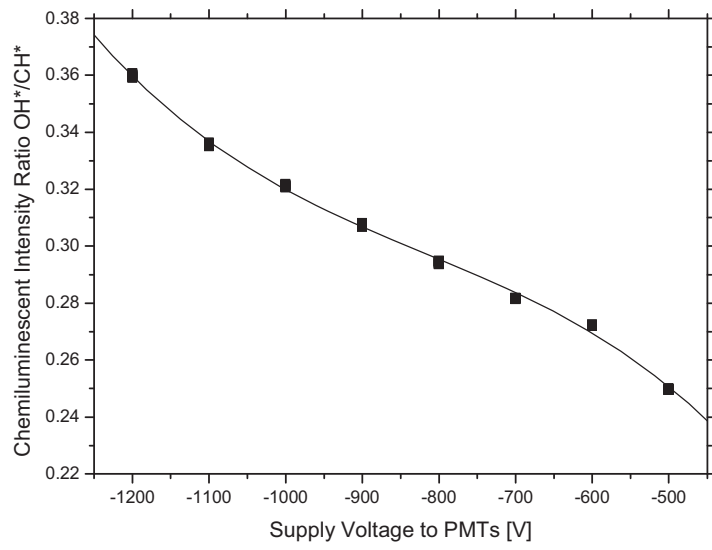


Fig. 20. Measured OH*/CH* chemiluminescent intensity ratio acquired from the Xe calibration lamp, as a function of the supply voltage to the detectors (PMTs). Line shows the polynomial fit to the measured data.

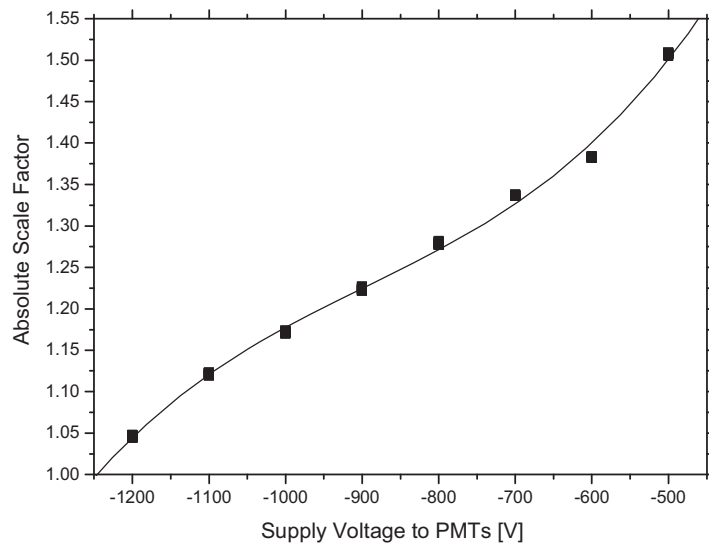


Fig. 21. Absolute scale factor used to convert measured OH*/CH* chemiluminescent intensity ratio to corrected values, as a function of the supply voltage to the detectors (PMTs). Line shows the polynomial fit to the measured data.